UNIVERSITAT ROVIRA I VIRGILI

COMPUTER SIMULATIONS OF RED BLOOD CELLS AND PROTEINS INTERACTING WITH NANOSTRUCTURED SURFACES

Berardo Mario Manzi

ADVERTIMENT. L'accés als continguts d'aquesta tesi doctoral i la seva utilització ha de respectar els drets de la persona autora. Pot ser utilitzada per a consulta o estudi personal, així com en activitats o materials d'investigació i docència en els termes establerts a l'art. 32 del Text Refós de la Llei de Propietat Intel·lectual (RDL 1/1996). Per altres utilitzacions es requereix l'autorització prèvia i expressa de la persona autora. En qualsevol cas, en la utilització dels seus continguts caldrà indicar de forma clara el nom i cognoms de la persona autora i el títol de la tesi doctoral. No s'autoritza la seva reproducció o altres formes d'explotació efectuades amb finalitats de lucre ni la seva comunicació pública des d'un lloc aliè al servei TDX. Tampoc s'autoritza la presentació del seu contingut en una finestra o marc aliè a TDX (framing). Aquesta reserva de drets afecta tant als continguts de la tesi com als seus resums i índexs.

ADVERTENCIA. El acceso a los contenidos de esta tesis doctoral y su utilización debe respetar los derechos de la persona autora. Puede ser utilizada para consulta o estudio personal, así como en actividades o materiales de investigación y docencia en los términos establecidos en el art. 32 del Texto Refundido de la Ley de Propiedad Intelectual (RDL 1/1996). Para otros usos se requiere la autorización previa y expresa de la persona autora. En cualquier caso, en la utilización de sus contenidos se deberá indicar de forma clara el nombre y apellidos de la persona autora y el título de la tesis doctoral. No se autoriza su reproducción u otras formas de explotación efectuadas con fines lucrativos ni su comunicación pública desde un sitio ajeno al servicio TDR. Tampoco se autoriza la presentación de su contenido en una ventana o marco ajeno a TDR (framing). Esta reserva de derechos afecta tanto al contenido de la tesis como a sus resúmenes e índices.

WARNING. Access to the contents of this doctoral thesis and its use must respect the rights of the author. It can be used for reference or private study, as well as research and learning activities or materials in the terms established by the 32nd article of the Spanish Consolidated Copyright Act (RDL 1/1996). Express and previous authorization of the author is required for any other uses. In any case, when using its content, full name of the author and title of the thesis must be clearly indicated. Reproduction or other forms of for profit use or public communication from outside TDX service is not allowed. Presentation of its content in a window or frame external to TDX (framing) is not authorized either. These rights affect both the content of the thesis and its abstracts and indexes.

UNIVERSITAT
ROVIRA i VIRGILI

Computer Simulations of Red Blood Cells and Proteins interacting with Nanostructured Surfaces

---

BERARDO MARIO MANZI

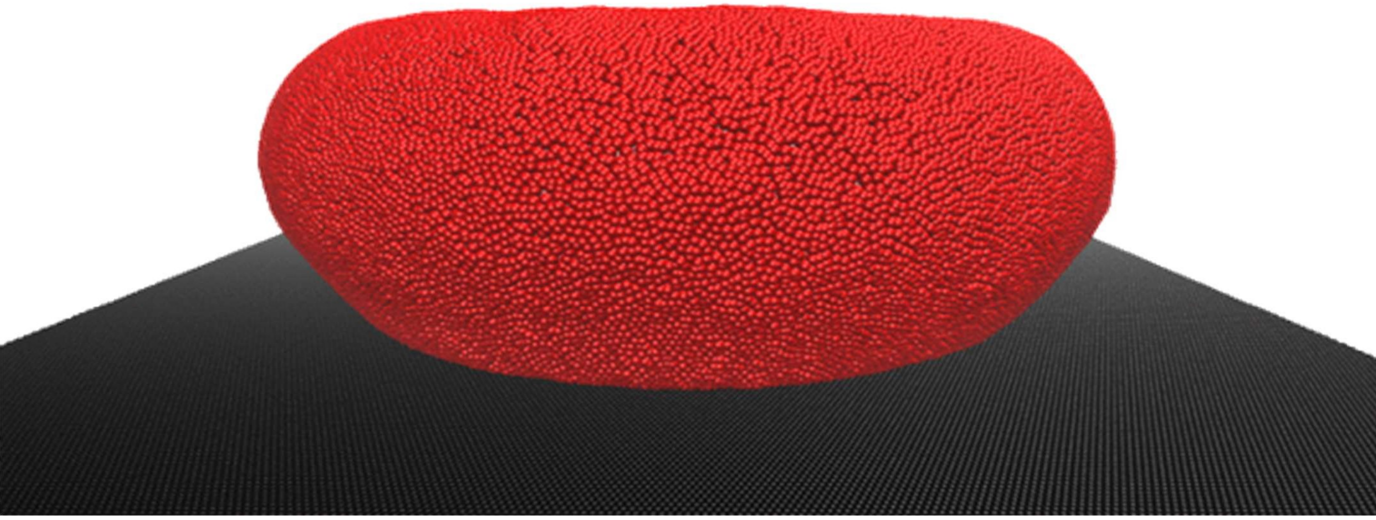

DOCTORAL THESIS

2018

Berardo Mario Manzi

Computer Simulations of Red Blood Cells and Proteins interacting with Nanostructured Surfaces

Doctoral Thesis

directed by Dr. Vladimir A. Baulin

ETSEQ

Tarragona 2018

UNIVERSITAT
ROVIRA i VIRGILI

Departament d'Enginyeria Química
Av. Països Catalans, 26
43007 Tarragona
Tel +34 977559700

I STATE that the present study, entitled "Computer Simulations of Red Blood Cells and Proteins interacting with Nanostructured Surfaces", presented by Berardo Mario Manzi for the award of the degree of Doctor, has been carried out under my supervision at the Department of Chemical Engineering of this university.

Tarragona, September 2018

Doctoral Thesis Supervisor

Vladimir A. Baulin

Acknowledgements

I like to thank my supervisor, Dr. Vladimir Baulin, for the opportunity to pursue this PhD, to the time devoted to the project and the uncountable hours spent solving all kind of issues. I also like to thank the other members of the group: PhD students Fabrizio Masullo, André Dias, Anna Orlowska, Dr. Adrien Berthault, Dr. Beibei Huang and Dr. Yachong Guo, for the numerous occasions of discussion and growth, and Dr. Marco Werner, Prof. Josep Bonet Avalos and Prof. Allan Mackie for sharing their expertise in computer simulations. Special appreciation goes to Prof. Elena Ivanova, which, despite the distance, always contributed to keep my project on track, and to Dr. Dmitry Fedosov, for providing the software for simulations of Red Blood Cells.

I am very grateful to all the people from the SNAL network, from the professors which, coming from several different fields, have introduced me to all kind of multidisciplinary knowledge, to the students, for the great personal and professional time spent together. In particular, I like to acknowledge Ankush Checkervarty, for his invaluable help in physical related topics, and Anna Sofia Tascini, a great support in both scientific and personal issues.

A comprehensive list of every person who made it possible for this work to exist is way too long, so I just like to thank all of them, from Jens-Uwe Sommer's group in Dresden, to all organisers of the SNAL events in Manchester, Roccalumera, Strasbourg, Frankfurt, London and Salou.

Administrative procedures represent always a burden, but I am very grateful to Núria Juanpere, the real backbone of the Chemical Engineering Department, and Teresa Mármol, who reminded me very often to never give up.

I like to thank my family for their support: my father Berardo Manzi and my mother Esther Oehninger, who lead me on this path from its very beginning, and my sister Patrizia Manzi with her family, Felix, Jasmine and Esteban Baez, for their patience, kindness and moral support.

Finally, my greatest thanks go to my fiancée, Fabiola Bonacci, who has never let me down, in all the late hours spent working, and whose support and love has been and is always immense.

Abstract

Recent advances in fabrication and modification of the nanotopography on surfaces have led to the development of a new generation of nanostructured materials with new properties, such as mechano-bactericidal activity and enhancement of growth of mammalian cells. This features are quite appealing for applications in biomedicine, especially as implants, but the underlying mechanisms driving the antimicrobial effects are not completely understood. Therefore, adequate theoretical modelling is required to provide deeper comprehension of the interactions between biological media and surfaces with nanoscale topographies.

This work presents two types of models, targeting two different aspects of the same problem. The first approach, Random Sequential Adsorption (RSA), describes the first step of any foreign entity entering the human body: protein adsorption. For this purpose, we develop an extension to RSA for nanostructured surfaces and show how complex geometries affect the final configurations of adsorption.

The second approach studies the actual interaction of cells with nanopatterned surfaces. We use Coarse-grained Langevin Dynamics to model deformations of Red Blood Cells, which represent an optimal compromise between computational simplicity and realistic modelling, and show how surfaces of different dimensions, including nanoparticles, affect the final shape of the cells. We demonstrate that the rupture is not caused by the piercing of the peaks on the surfaces, but rather by the important deformations leading to over-extension. This effect can be diminished by varying the design of the surfaces, in particular their dimensions.

Contents

Introduction

The importance of Biomaterials is growing at an increasing rate in both market share and fields of application. B. D. Ratner and S. J. Bryant[1] in 2004 reported a $100 billion endeavour concerning biomaterials, risen to $203.5 billion in 2013 and predicted to hit $400 billion in 2020.[2] Biomaterials are utilised in medical devices, such as heart valve prostheses, total hip replacement prostheses, dental implants, intraocular lenses, left ventricular assist devices,[3,4] but applications beyond the field of medicine are becoming more relevant, as exemplified by artificial compound eyes[5] and ship hull coatings.[6]

Despite the wide range of applications, the modern concept of biomaterial is relatively recent. Historically, medical implant materials have been exploited since millennia, with some archaeological evidence of sutures used over 32,000 years ago.[1,7,8] However, the associated issues related to infections and other biological reactions to these implants lead often to failure. The scientific approach to investigate biocompatibility of these materials has been initiated in the late 1940s by H. Ridley,[1] with the first implantation of poly(methyl methacrylate) lenses for replacing cataractous natural lenses.

Modern definitions of “Biomaterial” need to include a broad range of materials; D. Williams[9] defines a biomaterial as *a nonviable material used in a medical device, intended to interact with biological systems*, but, as already mentioned, the term “medical” can be dropped to include non-medical applications.

The materials used as biomaterials can be divided into two classes, synthetic and natural.[3,10] The former includes polymers (polyurethanes, silicones, flourinated biomaterials, acrylics), metals (Titanium, Stainless Steel), ceramics and glasses (synthetic hydroxyapatites, alumina), while the latter includes materials such as hyaluronic acid and collagen. Whatever the type and origin of the material, the degree of biocompatibility has to be assessed, which consists of testing toxicology, extrinsic organism colonization, mechanical effects (e.g. roughness) and cell-biomaterials interactions.[3]

The main focus of this work is a branch of the topic of biocompatibility: antibacterial surfaces. The colonization of biomaterials by bacteria is a major concern both in the preparation stage (sterilization) and following insertion (in case of implants).[11,12] In particular, these surfaces are commonly classified into two categories: antibiofouling surfaces, which prevent attachment of bacteria due to unfavourable morphology or surface coating, and bactericidal surfaces, which allow adhesion of bacteria, subsequently rupturing them.[11] An example of commonly employed biomaterial with antibacterial properties are Titanium and its alloys.[13] They represent a general preference for dental and orthopaedic implants, pacemakers, artificial hip joints and further applications due to the low electrical conductivity, high resistance to corrosion and high osteoconductivity. The main disadvantage of using Ti alloys is represented by the high Young modulus compared to the elastic modulus of human bone structure.[13] Moreover, after implantation, osteoconductivity has been shown to degrade over time,[14] reducing the compatibility with the bone tissue. Nevertheless, Ti and alloys such as Ti_6Al_4V are leading biomaterials in the aforementioned medical applications.

Despite the broad usage of Ti, the understanding of the underlying mechanisms which favour such materials over other candidates is far from complete. For instance, surface modifications at the micro-scale can enhance the biocompatibility of the implants.[15] Thus, the underlying topology of such surfaces appears to contribute significantly to the bactericidal or antifouling properties, and further research on micro- (and nano-) morphologies could give important insights.

Following this direction, new materials are being investigated: in particular, we are interested in recent discoveries of bactericidal effects of Black Silicon (bSi).[16] BSi is a variant of silicon which, due to its pillar like structures at the nanoscale, greatly suppresses light reflection, while increasing light scattering and adsorption efficiency.[17] The resulting appearance is thus black, and its properties, such as low reflectance, large active surface area and luminescence efficiency make bSi an optimal candidate for photovoltaic and optoelectronic applications, just to mention a few. Finally, the nanostructured surface also enhances bactericidal activity, compared to flat geometries, triggering a new branch of research for applications as biomaterial.

These discoveries of bactericidal activity of bSi were inspired by natural antibacterial surfaces such as insect wings, whose surfaces also present relevant topographies at the nano-scale.[18] One such example, Cicada wings, has been inspected both experimentally and theoretically. E. P. Ivanova et al. demonstrated mechanical rupture of *Pseudomonas aeruginosa* cells on *Psaltoda claripennis* wings, emphasising the special role played by geometrical features.[19] In fact, to explore the importance of surface chemistry, the originally highly hydrophobic wings were coated with a 10 nm thick gold layer, effectively reducing the original water contact angle from 158.8° to 105.5°, without significant change in the original topography. The bactericidal effect was preserved, proving that the physical structure, rather than the underlying chemistry, was primarily responsible for the mechanical rupture.

Having asserted the relevance of physical properties in bactericidal activity in experiments, theoretical models aimed at understanding such activity have been developed to provide significant information for the design of appropriate antibacterial surfaces. S. Pogodin et al.[20] analyse the free energy of stretching upon contact of bacteria with nanopillars, proposing a possible mechanism of cell membrane rupture. Analogously, Li[21] used a thermodynamic model to describe the bactericidal mechanism of nanostructures on disk shaped cell membranes. Despite significant insight provided by such approaches, a more comprehensive study is required if these surfaces have to be employed for medical applications, given the complexity of the environment in the human body.

The present work aims to address several aspects of the interactions between biomaterials and the biological media in which they are inserted. In particular, proteins first populate any foreign object entering the human body.[22] Red Blood Cells (RBCs) will definitely enter in contact at some point with the external material and are expected to survive the event, while bacteria should be ruptured by the bactericidal surface. Each of these phenomena have been simulated using different methods, and a brief introduction is given in the following paragraphs.

Protein adsorption on nanostructured surfaces

Blood plasma is constituted by several hundreds of protein species,[23] with Human Serum Albumin (HSA), immunoglobulins type G (IgG), transferrin (Tr), Fibrinogen (Fib) and immuonglobulins type A (IgA) representing the most abundant ones. Upon insertion of a foreign body in the blood stream, surface colonisation will occur, with the smaller proteins, such as HSA, preceding larger ones, e.g. Fib, which will than replace the former due to stronger interface interactions (Vroman effect).[24] The attachment is considered generally irreversible or almost irreversible, although ongoing debates exist in different scientific communities.[23] Nevertheless, concerning smaller proteins, in particular HSA, the agreement on irreversible adsorption is quite general, and allowed us to perform computer simulations with this assumption.

Theoretical approaches to the problem of protein adsorption, given its complexity, are generally quite limited. The most misleading method used for analysis of isotherms is Langmuir adsorption,[25] originally developed for gas adsorption on porous media. In fact, the working hypotheses of this approach are:

- All adsorption sites on the surface are equivalent
- Only one molecule can adsorb onto a given site at any time (no overlap of molecules allowed)
- No interaction is present between adsorbing molecules
- The process of adsorption is **reversible**

These conditions are limiting the predicting power of the model, with special emphasis on the assumption of reversibility, which is in clear contradiction with the aforementioned irreversibility of protein adsorption. However, most likely due to its simplicity, the Langmuir approach is still quite widespread, inducing misinterpretation of experimental results.[26]

A sounder method is the Random Sequential Adsorption (RSA) approach,[27] also named the "Car-parking problem". The method consists of sequential attempts to adsorb a generic particle to an N-dimensional manifold (a line in 1-D, a surface in 2-D or a volume in 3-D), with problem-specific constraints for latter particle positioning. For instance, J. Feder performed RSA simulations of disk on a flat surface, applying a simple steric repulsion constraint, i.e. placement of a particle may occur solely if not overlapping with previously adhered particles.[28]

Analytical solutions for RSA are available only in the 1-D case; in higher dimensions numerical calculations or computer simulations are necessary. A very common method relies on Monte Carlo (MC) steps, in which a particle is generated at a random position on the surface and adheres if the constraint is satisfied, otherwise the attachment is rejected. Several authors have approached the topic in this fashion: from steric repulsion constraint for disks on flat surfaces,[28] to linear chains adsorption as Fib models,[29] to hard sphere adsorption to a volume.[30]

Theoretical models of protein adsorption on nanostructured surfaces are important to achieve a comprehensive understanding of the preservation of the bactericidal effect in blood stream. Excessive amount of protein could saturate the surface, smoothing the topography causing the rupturing effects. To our knowledge, protein adsorption to nanostructured surface, which we present in this work, appears to have been overlooked in previous studies. We show results obtained using computer simulations, in analogy to former studies, adapting the MC RSA approach to the new geometries. In part I the theoretical background for RSA is elucidated, with particular care for the modifications introduced. Then, in part II, we demonstrate our findings, and the conclusions which can be inferred from the simulations.

RBCs interacting with nanopatterned surfaces and solid nanoparticles

The second focus of our work concerns Red Blood Cells (RBCs). In fact, the promising features of bactericidal properties of bSi (and Cicada wings), and the low toxicity of these surfaces for mammalian cells, is juxtaposed to the unwanted rupturing effect on RBCs.[31] Such rupturing effects on RBCs and bacteria suggest a possible length scale dependence of the bactericidal activity, since RBCs are among the smallest mammalian cells ($6 - 8$ µm),[32] compared to typical ~ 10 µm scales of more complex cells). Obviously, if protein adsorption, mentioned in the previous section, would inhibit the bactericidal effect of nanostructures, the RBCs rupture would also be negated. However, this represents an undesired case, and, moreover, we demonstrate that it does not occur. Therefore, it is more important to understand what length scales of the underlying topology induce mechanical rupture on RBCs, and to suggest adequate design to the surface producers. Fortunately, the task is facilitated by the relatively simple structure of RBCs, for which solid computational models exist.[33, 34]

We investigate interactions of RBCs with flat surfaces, Cicada wings and bSi using the theoretical framework developed by D. A. Fedosov et al.[33] Their approach models RBCs as triangulated surfaces, whose vertices move according to Dissipative Particle Dynamics (DPD),[35, 36] with a potential defined to correctly take into account the viscoelastic behaviour of the outer lipid membrane and the underlying spectrin network.[37] Details of the theoretical framework will be outlined in chapter 2, where we also discuss the rationale behind our choice to use Langevin dynamics[38] instead of DPD.

Following the results about protein adsorption in chapter 3, we outline the outcome of the simulations of RBCs on different nanostructured surfaces. We will extract information about membrane deformations by solving a topologically equivalent problem, nanoparticle adsorption on RBCs, while reducing the computational cost involved in the simulations. Analysing the strain-stress relations we observe that strong deformations leading to inclusion of foreign bodies, either nanoparticles or nanopillars, is not possible, due to the elastic properties of spectrin network. However, several piercing objects lead to an overall tensile deformation and possible rupture.

Part I

Theoretical methods

Chapter 1

Models for Protein Adsorption on nanostructured surfaces

The interaction of Proteins with solid interfaces is a topic of great relevance in the study of biomaterials, nanotechnologies and beyond.[39] Despite the importance, theoretical models are often strong approximations and aimed to describe a specific feature, thus with little or no generalisation power. Kinetic models (Langmuir adsorption isotherms, RSA) are capable to output quantities such as the saturation limit distribution and pair correlation functions,[27,40] while unable to predict information about the timescales of the processes involved, unless coupling with other methods, such as diffusion equation computation,[41] is exploited. Conversely, Molecular Dynamics approaches are suitable for extraction of realistic time dependent quantities, although extremely coarse-grained force fields are required to keep the computational resources affordable.[42] In fact, full atomistic resolution of a single protein contains thousands of heavy atoms (excluding Hydrogen), while coarse-graining at the amino acid scale still requires several hundreds of beads per protein. For instance, the Humans Serum Albumin (HSA) crystallographic structure shown in figure 1.1 and obtained via X-Ray diffraction,[43] contains 9205 atoms, in a sequence of 585 amino acids. Therefore, the selected method is necessarily a compromise, given the type of information requested, as is the chosen level of coarse-graining. In the following, all methods will treat the proteins as spherical particles, which is a reasonable and frequently utilised assumption for cases such as HSA;[23,44] for more complex proteins, e.g. Fibronectin (Fib) different assumptions would be necessary, but were beyond the scope of our work.

A method which receives great criticism, despite its widespread use, is the Langmuir adsorption isotherm approach.[26] Its use, originally developed for **reversible** gas adsorption on porous media,[25] as model for protein adsorption results in misleading conclusions. More suitable is the Random Sequential adsorption (RSA) approach,[27] which explicitly assumes **irreversibility** of protein adhesion.

The following sections will outline both methods, explaining how to extract the relevant quantities. Langmuir adsorption is considered for mere comparison with other methods in part II, and to once again highlight the erroneous interpretation of the results obtained via

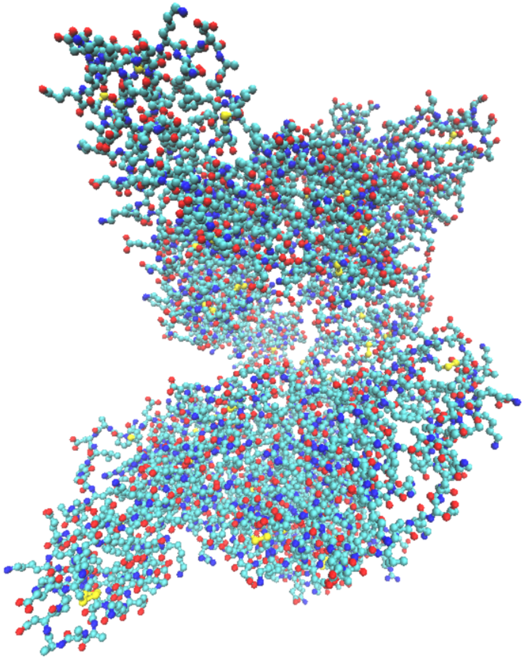

Figure 1.1: Human serum albumin at full-atom resolution. Colour scheme is red for O, blue for N, cyan for C and yellow for S. Snapshot obtained using Visual Molecular Dynamics (VMD)[45] software, with data available at the RCBS Protein Data Bank (PDB) website (`https://www.rcsb.org`).[43]

this approach.

1.1 Kinetics of protein adsorption

The adsorption of N spherical particles of cross-section $\pi\sigma^2/4$ onto a surface of area A, can be described via the time dependence of the occupancy $\theta(t) = N(t)\pi\sigma^2/4A$, using the equation:[46]

$$\frac{d\theta}{dt} = k_a n B(\theta) - k_d \theta. \tag{1.1}$$

Here, k_a and k_d are the constants of adsorption and desorption, respectively, n is the volume density of particles in the bulk, and $B(\theta)$ is the *surface exclusion effect*, or *Blocking* function at a given occupancy θ. The density n is supposed to be constant throughout the adsorption process, approximation which holds as long as the number of proteins in the bulk of the solution is much greater than on the surface.

The blocking function $B(\theta)$ represents the probability for a particle to adsorb, for a given amount of particles already present on the surface. Naturally, $B(\theta)$ will equal unity when the surface is empty, and will decrease with increasing occupancy θ. For Langmuir adsorption, $B(\theta) = 1 - \theta$ or $B(\theta) = \theta_\infty - \theta$ for adsorption on a discrete number of sites or a continuous surface, respectively. Following an initial transient time for protein colonisation on the surface, a dynamic equilibrium between adsorption and desorption will be reached. Setting $d\theta/dt = 0$ in equation 1.1 yields:

$$\theta = \frac{K_{eq} n}{1 + K_{eq} n} \theta_\infty, \tag{1.2}$$

where $K_{eq} = k_a/k_d$ and $\theta_\infty = 1$, if the surface is constituted of a finite amount of sites. The typical behaviour of a Langmuir isotherm is reported in figure 1.2a, with $K_{eq} = 1.73 \cdot 10^7$ L/mol[26] and $\theta_\infty = \pi/2\sqrt{3} \simeq 0.9069$, corresponding to closed hexagonal packing. The assumption of achieving a uniform packing is confirmed by the theory of reversible adsorption and by experimental observations,[47] and the value for θ_∞ can be computed as the ratio of the area of three slices of spheres inside the red triangle in figure 1.2b and the area of said triangle.

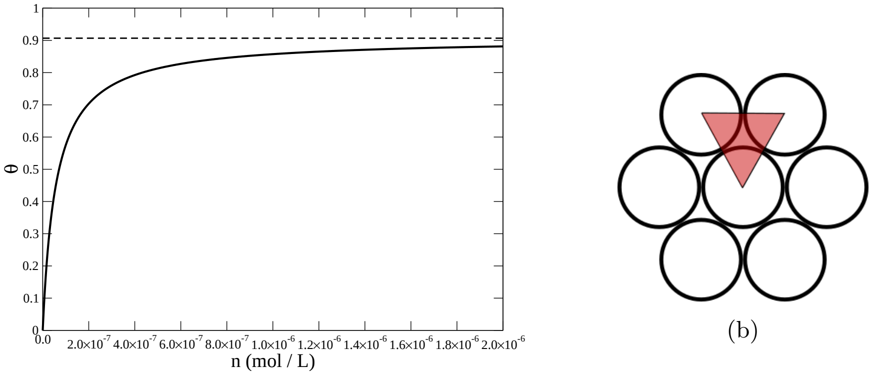

(a)

(b)

Figure 1.2: (a) Shape of the Langmuir adsorption isotherm of equation 1.2, with $\theta_\infty = 0.9069$, asymptotic value estimated for adsorption on continuous surfaces, assuming hexagonal packing, as in (b). The value for θ_∞ can be calculated as the ratio of the area of the three circle sections included in the red triangle and the area of said triangle.

The initial steep increase, followed by an asymptotic trend towards saturation is a commonly observed behaviour of the protein adsorption mechanism,[47, 48] and is quite often the only justification for the utilization of Langmuir approach.[26] In chapter 3 we will discuss the limitation of such reasoning by comparing it with RSA.

Noteworthy is the dependence of protein adsorption on sphere packing, a well known and complex problem.[49] A general approach to the Kepler conjecture is far beyond the scope of this work, but nevertheless a few considerations are mandatory to adequately interpret the results of our computations in chapter 3. Therefore, in the following section, we discuss the effect of curved surfaces on dense sphere packing, which will be a recurrent topic while analysing our observations.

1.2 Sphere packing problem on curved surfaces

The argument in this section is treated for a one dimensional case for the sake of simplicity. Considerations for the case of adsorption on two dimensional manifolds are straightforward generalisations of the former, and analogous conclusions can be deduced.

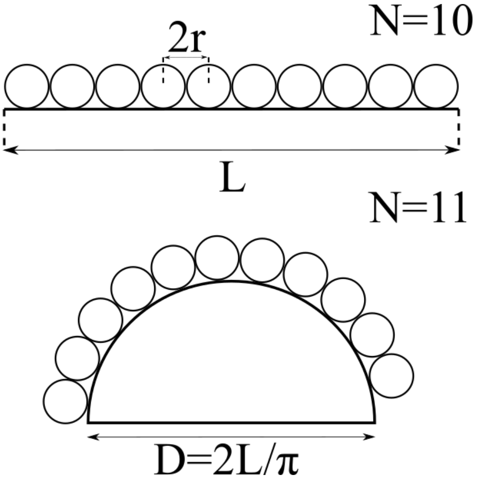

Figure 1.3: Comparison of circle packing on a line segment versus a semicircle. Ten circles of diameter $\sigma = 2r = L/10$ can be placed on a line of length L, while more than 11 fit onto the semicircle of the same length (i.e. diameter $D = 2L/\pi$).

Figure 1.3 illustrates a case where 10 spheres (or their circular section) are placed at closed packing on a line segment of length $L = 10\sigma$, with $\sigma = 2r$ the diameter of a sphere. From the second image it is evident that the convex hemisphere, whose (semi-) circumference is also L, allows more spheres to fit, due to the lower occupancy of a single sphere. In fact, defining $N_{f_{max}} = L/\sigma$ and $N_{s_{max}} = L/s$ as the maximum amount of spheres fitting on the line and on the hemisphere, respectively, and being s the arc length effectively occupied by a single sphere, we have:

$$s = \alpha R = 2 \arcsin\left(\frac{r}{R+r}\right) R. \tag{1.3}$$

The relation for α is obtained from the construction in figure 1.4. The condition for lower occupancy on the curved surface is $s < 2r$, or, equivalently:

$$\frac{r}{r+R} < \sin\left(\frac{r}{R}\right). \tag{1.4}$$

Under the condition that $r < R$, $\sin(r/R) < \sin(1) \simeq 0.84$, and lower occupancy is achieved if:

$$r \lesssim 5.25R, \tag{1.5}$$

which certainly holds given $r < R$. An analogous argument leads to conclude that, for concave surfaces, the occupancy is lower than for flat ones.

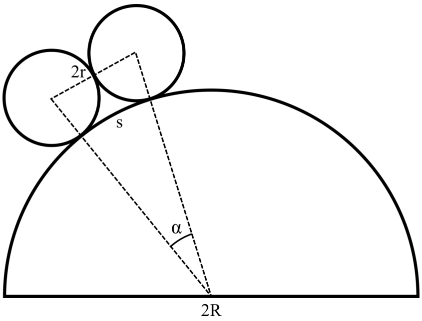

Figure 1.4: Geometry defining equation 1.3.

This apparently simple argument is often overlooked in protein adsorption on more complex topologies,[48] and the lack of proportionality between the increase in number of adsorbed proteins and area increase is attributed to diffusive, dynamic or other physical phenomena not under direct control of the observer. Evidently, occupancy does not change on larger area, being it a quantity defined per unit area; any of such changes, if not conformational, is therefore related to curvature.

The inclusion of curvature effects in the Langmuir theory of adsorption is achieved by a change of θ_∞, or, conversely, any measurement of θ_∞ will highlight a change of topology of the underlying surface. In the case of RSA, described in the next section, the Blocking function $B(\theta)$ will be affected, but the curvature dependence is implicit in the model.

1.3 Random Sequential Adsorption

The Random Sequential Adsorption method is based on A. Rényi's *Car-parking* problem,[50] which describes the placement of cars along a given line. The situation, displayed in figure 1.5, consists of placing "cars" (represented as rectangles in the figure) at a random spot along the line, without overlapping of subsequent rectangles. For instance, in the illustrative example of figure 1.5, three cars are already placed along the line, with formation of unavailable empty space between cars 1 and 2, which, thus, constrains car 4 to park in between cars 2 and 3. Formally, the average amount of cars $M(x)$ which fit onto interval $\mathcal{I} = [0, x]$, $x > 1$ and assuming all cars to be of unit length, can be computed analytically.[51] Consider the first car, parked at $[t, t+1] \subset [0, x+1]$; the average number of cars at its left is $M(t)$ and the average number of cars at its right is $M(x-t)$. Given that t is drawn from a uniform distribution on $\mathcal{I}$ we can write:

$$M(x+1) = \frac{1}{x}\int_0^x \left(M\left(t\right) + M\left(x-t\right)\right)dt + 1 \tag{1.6}$$

or equivalently:

$$M(x) = 1 + \frac{2}{x-1}\int_0^{x-1} M(t)dt \tag{1.7}$$

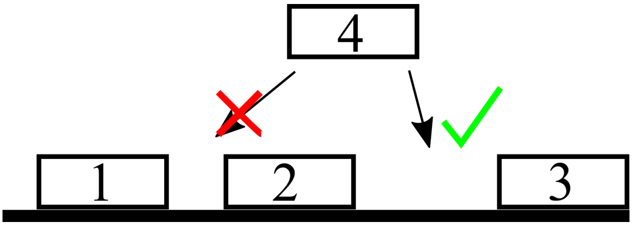

Figure 1.5: Illustrative example of "Car" placement along a line. Following the parking of cars 1 to 3, some empty space has been created, in which no other car fits (between cars 1 and 2), although car 4 will still fit between cars 2 and 3. The final occupancy of a line segment upon RSA will generally satisfy the relation $\theta_\infty < 1$.

with $M(x) = 0$ if $0 \leq x < 1$. The mean density of cars for $x \to \infty$ assumes the value:[27,51]

$$m(x) = \lim_{x\to\infty} \frac{M(x)}{x} = \int_0^\infty \exp\left(-2\int_0^x \frac{1-e^{-y}}{y} dy\right) dx = 0.7475979202\ldots \tag{1.8}$$

and called *Rényi's Parking Constant*, after the author of its first derivation. The rather cumbersome computation leading to equation 1.8 is not reported here for the sake of brevity.

It is noteworthy to highlight the assumptions used in the derivation of the relation for the Car-parking problem: non-overlapping rectangles and cars of equal length. The former is compulsory in case of RSA applied to solid objects, such as cars, but is not straightforward for soft matter systems such as protein adsorption. The second assumption represents a limitation even for the case of car parking: commonly, cars of different sizes would park along a given roadside. Nevertheless, the 1-D model introduces some important concepts, typical of RSA, which are used in higher dimensions, and for more complex systems. Perhaps the most relevant is the saturation limit θ_∞, indicated as $m(x)$ in equation 1.8, which represents the coverage achieved for $t \to \infty$, i.e. when no other particles can be adsorbed. Evidently, $\theta_\infty < 1$, and common values for simple geometries also satisfy $\theta < m(x)$. Another important factor is the trend of adsorption, with straightforward adhesion of the first particle, while the line (or a higher dimensional surface) is empty, and with decreased probability of adsorption as the occupancy grows closer to θ_∞.

Having illustrated the simplest case of 1 dimensional RSA, we will move to the more interesting case of 2-D adsorption, which is the most relevant for protein adsorption processes treated in this work. Previous works addressed the RSA problem under different assumptions. J. Feder[28] considered solid disks and aligned squares adsorbing to a flat surface, computing the values of $\theta_\infty = 0.547 \pm 0.002$ and $\theta_\infty = 0.562 \pm 0.002$, respectively. Z. Adamczyk and P. Weroński[52] consider RSA of spheroidal particles, as a function of aspect ratio, while B. Widom[30] studied adsorption of particles to a volume. All these works perform numerical simulations, as an analytical solution is not known for such complex cases.[27]

The numerical method used in this work is an extension of the approaches of J. Feder[28] and of P. Schaaf and J. Talbot:[46] we consider proteins, approximated as spheres, and let them adsorb using a Monte Carlo (MC) approach. Each MC step consists of drawing a set of (x, y) coordinates from a uniform distribution and attempting to place a particle i to the point. If the placement satisfies the constraints, the MC move is accepted, otherwise a new set of coordinates is drawn, until successful collocation. Then, the number of attempts n_i is recorded and the probability of adsorption defined as:

$$p_i = \frac{1}{n_i}. \tag{1.9}$$

Obviously, p_i will depend on the particular configuration of the surface due to the $i-1$ proteins already adsorbed, and, thus on a series of random events, which are not reproducible if repeated. In fact, we are interested in statistical significant results, and for this purpose, each simulation is repeated a certain amount of times N. In other words, equation 1.9 becomes:

$$p_i = \frac{1}{\langle n_i \rangle}, \tag{1.10}$$

with:

$$\langle n_i \rangle = \frac{1}{N} \sum_{r}^{N} n_{i,r}. \tag{1.11}$$

The function defining the probability of adsorption at a given occupancy θ is the aforementioned blocking function $B(\theta) = p_i(\theta)$,[40] and can be used to solve equation 1.1.

The blocking function obtained via the approach outlined thus far is a numerical approximation of the real theoretical function. The data obtained from the simulations can be used to fit $B(\theta)$ as a polynomial $\sum_m^n a_m \theta^m$, and each order of the expansion has been shown to carry information about the configuration of adsorbed proteins.[46] Starting with an empty surface, the probability to adsorb at $\theta = 0$ is $B(\theta = 0) = 1$, as any attempt will automatically succeed. Considering hard spheres of diameter σ, each particle will exclude an area, due to steric repulsion, equal to 2σ, since no centres of subsequent particles can be placed without overlap, as illustrated in figure 1.6 (external ring represents excluded area). Therefore, the excluded area will behave as $B(\theta) \sim 1 - N(\theta)/A\pi\sigma^2 = 4\theta$, where N is the number of adsorbed disks on the surface, A is the total area of the surface and $\theta = N/A\pi\sigma^2/4$ is the occupancy. Second order contributions take into account double counting of overlapping excluded areas, as depicted in figure 1.7. The common area $A_2(\mathbf{r}_i, \mathbf{r}_j)$ of particles i and j will depend only on the relative distance $r_{ij} = |\mathbf{r}_i - \mathbf{r}_j|$, and will be denoted as $A_2(r_{ij})$. The number of pairs $N_2(r_{ij})$ with centres distances between r_{ij} and $r_{ij} + dr_{ij}$, in case of *nearly* randomly distributed particles, and at low density is:[46]

$$N_2(r) = \frac{1}{2}\left(2\pi r \frac{N^2}{A^2} + \mathcal{O}\left(\left(\frac{N}{A}\right)^3\right)\right) \tag{1.12}$$

yielding a second order correction factor:

$$S_2 = \frac{N^2}{2A^2} \int_{\sigma}^{2\sigma} 2\pi r A_2(r) dr \tag{1.13}$$

to be **added** to $B(\theta)$.

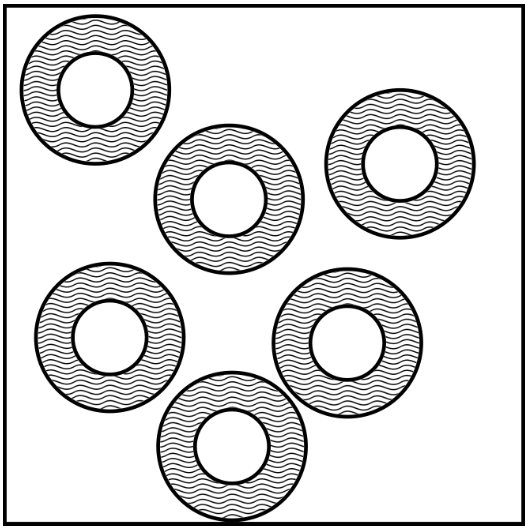

Figure 1.6: Example of initial disks adsorption on a flat surface, with representation of the excluded area surrounding each disk.

The general expression for higher order corrections is:[53]

$$B(\theta) = 1 - S_1 + S_2 - S_3 + \dots, \tag{1.14}$$

where

$$S_n = \frac{1}{n!}\int\int\cdots\int \rho^{(n)}(\mathbf{r}_1, \mathbf{r}_2, \dots, \mathbf{r}_n) A_n(\mathbf{r}_1, \mathbf{r}_2, \dots, \mathbf{r}_n) d\mathbf{r}_1 d\mathbf{r}_2 \dots d\mathbf{r}_n, \tag{1.15}$$

and where $\rho^{(n)}(\mathbf{r}_1, \mathbf{r}_2, \dots, \mathbf{r}_n)$ is the n particle distribution function ($\rho^{(2)}(\mathbf{r}_1, \mathbf{r}_2)$ is the pair correlation function), and $A_n(\mathbf{r}_1, \mathbf{r}_2, \dots, \mathbf{r}_n)$ the overlapping area of the n neighbouring particles. In analogy with P. Schaaf and J. Talbot[46] we will expand $B(\theta)$ to third order, therefore including contributions of the form illustrated in figure 1.8, which take into account the formation of additionally excluded areas, like the red area in the image.

A comment is mandatory at this point. We have not discussed other constraints for the RSA process except avoidance of overlapping between spheres. In fact, equations 1.12-1.15 are derived under the approximation of hard spheres for the adsorbate, with no interactions between particles of the adsorbing species. This is generally in good agreement with weakly clustering proteins such as HSA,[23] and will be assumed in the remaining of this work.

Finally, the results in chapter 3 will concern non trivial topologies, contrarily to the examples illustrated thus far. Although effects similar to the ones discussed in section 1.2 are implicit in the shape of the blocking function $B(\theta)$ and in the value for θ_∞, care has to be taken for the generation of the particles on the surface. As discussed earlier, disks (or spheres) have to be uniformly placed on top of the surface. For flat geometries this is equivalent to generate 2 random numbers x, y on the domain of the surface, since the

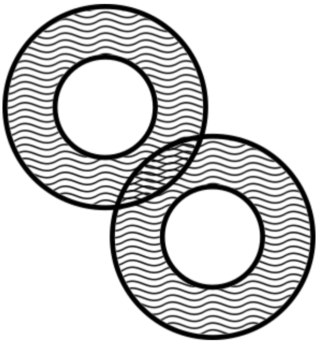

Figure 1.7: Representation of a second order exclusion contribution to $B(\theta)$, which needs to take into account of the overlapping of the shaded regions, to avoid double counting.

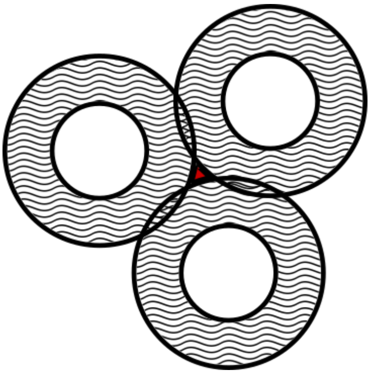

Figure 1.8: Representation of a third order exclusion contribution to $B(\theta)$ (area in red).

metric tensor equals the identity matrix. However, for more complex geometries, the metric becomes:[54]

$$g_{ab} = \begin{bmatrix} 1 + \frac{\partial^2 h}{\partial x^2} & \frac{\partial h}{\partial x}\frac{\partial h}{\partial y} \\ \frac{\partial h}{\partial x}\frac{\partial h}{\partial y} & 1 + \frac{\partial^2 h}{\partial y^2} \end{bmatrix} \tag{1.16}$$

where we utilised the *Monge* gauge:

$$\mathbf{r} = \begin{bmatrix} x \\ y \\ h(x,y) \end{bmatrix} \tag{1.17}$$

with $h(x,y)$ being the analytical expression for the surface. The condition for uniform distribution on the generic surface $z = h(x,y)$ is that each area element dA of the surface is equally probable. In other words:

$$dP \propto dA = \sqrt{g} dx dy \tag{1.18}$$

with $g = 1/2 \sum_{a,b,c,d} \epsilon^{ab} \epsilon^{cd} g_{ab} g_{cd}$, a, b, c, $d \in \{x, y\}$ and ϵ^{ab} the two dimensional Levi-Civita symbol $\epsilon^{xx} = \epsilon^{yy} = 0$, $\epsilon^{xy} = -\epsilon^{yx} = 1$. In practice, since inversion of this expression is required to define a random number generator, and since such inversion becomes hard, if not impossible to perform in the general case, we used a numerical approach: every time a position (x, y) is uniformly generated, the position is selected if and only if a randomly generated number $r \in [0, \sqrt{g_{max}}]$, with g_{max} the maximum value for g, satisfies $r < \sqrt{g}$; otherwise a new position is generated. In other words, the generation of the positions follows a MC scheme.

Chapter 2

Simulation of Triangulated surface adhesion using Langevin Dynamics

The mechanics of soft objects such as bacteria, lipid vesicles and cells in general plays a fundamental role in the exploration of the properties of biomaterials. The triggers for our work were represented by observations of rupturing effects of *Pseudonomas Aeruginosa*,[16,19] *Bacillus Subtilis*, *Planococcus maritimus* and *Staphylococcous aureus*[16,20] on different types of natural and artificial nanopatterned surfaces, such as cicada (*Psaltoda Claripennis*) wings and Black Silicon (bSi). Additional observations of erythrocyte lysis,[31] motivated the computational exploration of these mechanisms to attempt to understand them. The use of computational tools appears quite appealing, given the independence of the underlying rupturing effects from the chemical composition of the surfaces.[19,20] Therefore, an approach from a physical perspective seems to be the most appropriate.

Comprehensive computational models capable of describing cells in detail are, to date, infeasible. The amount of complexity at the atomic scale, as for the case of proteins outlined in the introduction to chapter 1, is way beyond the power of modern computer systems, and simplifications are generally performed,[55] according to the interested type of information. For instance, studies about lipid bilayers have been tackled using various approaches, from Molecular Dynamics (MD) simulations at different levels of coarse-graining, to Monte Carlo (MC) simulations, to numerical calculations of free energy.[56–58] Blood flow and RBCs have been simulated with both continuum and discrete methods,[59,60] where the level of coarse-graining is even greater.

We employ coarse-grained MD simulations of RBCs adhering to surfaces, as well as nanoparticles adsorbing to RBCs, to test their mechanical properties. Such choice is often preferred to other approaches[61,62] for both its computational stability and the possibility of observing non equilibrium effects in the dynamics of cells. Moreover, sound models have already been developed and tested for correctly predicting the outcome of experiments.[33,34] One of this model, due to D. A. Fedosov, B. Caswell and G. E. Karniadakis[33] will be described in the following sections, as it has been used, with slight modifications, for our computations of RBC adhesion.

The next section will review some basic concepts of MD, with special emphasis on the Langevin equations, used as a thermostat in our calculations. Next, we describe the force-field used for our triangulated meshes of RBCs and explain the relations between the parameters of the model and the macroscopic properties.

2.1 Overview of Molecular Dynamics and Langevin Dynamics

MD simulations aim to predict macroscopic information from the dynamics of microscopic particles, in accordance with the statistical theory of Boltzmann.[38] Given the hamiltonian $\mathcal{H}$ of a system, and given the equations of Hamilton:

$$\dot{q}_i = \frac{\partial \mathcal{H}}{\partial p_i} \tag{2.1}$$

$$\dot{p}_i = -\frac{\partial \mathcal{H}}{\partial q_i} \tag{2.2}$$

where q_i and p_i are the generalised coordinate and momentum of particle i, thermodynamic quantities can be extracted as mean values over the set of all particles, in the limit of large number of particles $N \to \infty$. For instance, the temperature of an ensemble of particles can be computed from the equipartition theorem:

$$\delta_{mn} k_B T = \langle q_m \frac{\partial \mathcal{H}}{\partial q_n} \rangle \tag{2.3}$$

where k_B is the Boltzmann constant and δ_{mn} the Kronecker delta, which is 1 if $m = n$ and 0 otherwise.

In principle, finding a solution for equations 2.1-2.2 for all particles in a system and computing the desired quantities as averages is all what MD is about. In practice, there are several aspects which have to be considered when working on a computational model for statistical mechanics. First, the aforementioned condition $N \to \infty$, or at least $N \propto N_A$, where $N_A \simeq 6.022 \cdot 10^{23}$ is the Avogadro number, can not be satisfied in nowadays computers; common amounts of particles being simulated can reach 10^6, perhaps 10^7, much smaller than the thermodynamic limit. Placing such a small amount of particles into a finite sized box of volume V would not appropriately reproduce the bulk properties of a macroscopic system, due to the presence of fixed boundary conditions. Similarly, the removal of any boundary conditions (free, interacting particles) would cause a rapid dispersion of the particles, with no remaining interaction. Therefore, periodic boundary conditions are generally employed, with particles exiting one side of the simulation box re-entering the other side, as shown in figure 2.1.

Moreover, the small number of degrees of freedom in simulated systems can not, in general, reach real values of the macroscopic thermodynamic observables, e.g. temperature, and external sources have to be added to the hamiltonian $\mathcal{H}$ to obtain the correct

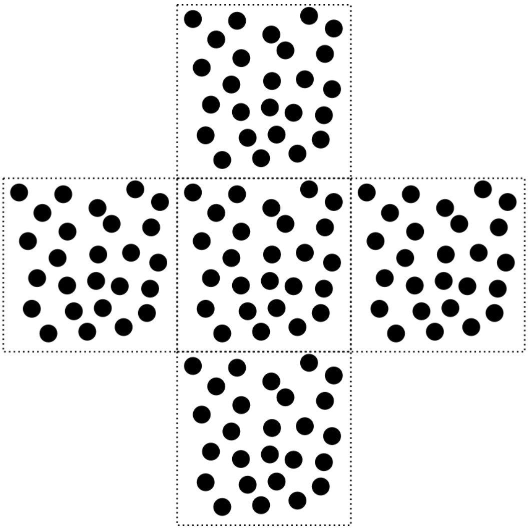

Figure 2.1: Original system (center) and periodic images, for a 2D particle simulations. All particles and their images move identically, and every time a particle leaves the box on a side, its image on the opposite side enters.

macroscopic ensemble.[38] For instance, a typical choice for a canonical ensamble is the Nosé-Hoover thermostat:[63]

$$\mathcal{H} = \sum_{i=1}^{N} \frac{\mathbf{p}_i^2}{2m_i s^2} + \sum_{i<j} V\left(\mathbf{r}_i - \mathbf{r}_j\right) + \frac{p_s^2}{2Q} + g k_B T \log(s) \tag{2.4}$$

where the additional degree of freedom s represents the thermostatting variable and p_s its conjugate momentum, and we have specialised to Cartesian coordinates $\{\mathbf{r}_i, \mathbf{p}_i\}$. The coordinates in equation 2.4 are virtual coordinates, and are linked to the real coordinates via the relations:

$$\mathbf{r}'_i = \mathbf{r}_j, \quad \mathbf{p}'_i = \frac{\mathbf{p}_i}{s}, \quad dt' = \frac{dt}{s}, \quad s' = s, \quad p'_s = \frac{p_s}{s}, \tag{2.5}$$

with the primed quantities being the real ones. Finally, defining:

$$\eta = \log(s), \quad p_\eta = Q\frac{1}{s}\frac{ds}{dt'} \tag{2.6}$$

leads to the equations of motion:

$$\dot{\mathbf{r}}'_i = \frac{\mathbf{p}_i}{m_i}, \tag{2.7}$$

$$\dot{\mathbf{p}}'_i = \mathbf{F}_i - \frac{p_\eta}{Q}\mathbf{p}'_i, \tag{2.8}$$

$$\dot{\eta} = \frac{p_\eta}{Q}, \tag{2.9}$$

$$\dot{p_\eta} = \sum_{i=1}^{N} \frac{\mathbf{p}'^2_i}{m_i} - g k_B T. \tag{2.10}$$

The last equation highlights the role of the new coordinate, since the momentum p_η will minimise the difference between the kinetic energy of all particles and the thermodynamic limit requested by the equipartition theorem.

Different types of thermostats are possible and the particular choice will depend on the type of system we intend to simulate. Having very coarse-grained entities, where it is desirable to reduce the DoFs as much as possible, we chose to use a set of equations of motions which does not include explicitly molecules of water. The *Generalised Langevin Equations*:

$$m_i \ddot{q}_i(t) = F_i(q_i(t)) - \gamma \dot{q}_i(t) + R_i(t) \tag{2.11}$$

represent such a set of relations, where:

$$F_i(q_i(t)) = -\frac{\partial V}{\partial q_i} \tag{2.12}$$

is the force acting on particle i, γ is the viscous damping coefficient and $R(t)$ is a random force. The use of a stochastic term in a deterministic approach might appear misleading, but we remind that the role of a thermostat, or *thermal bath*, is to smooth the dynamic of a single (microscopic) particle to consistently achieve an overall (macroscopic) thermodynamic ensemble. It can be shown that, as long as the *second fluctuation dissipation theorem*:[38, 64]

$$\langle R(0)R(t)\rangle = k_B T \gamma \delta(t), \tag{2.13}$$

with $\delta(t)$ the Dirac delta, is satisfied, a canonical ensemble for particle i will be obtained.

The equations presented thus far are in their analytical and continuous form, despite the incapability of computer systems to treat functional equations. Indeed, MD simulations evolve following an approximation scheme, which unavoidably introduces further numerical errors. The theory of numerical integrators, as well as some common examples such as the Verlet[65] or leapfrog algorithms, is beyond the scope of this work. However, the numerical integrator of equations 2.11 is reported here, based on the derivation of E. Vanden-Eijnden and G. Ciccotti:[66]

$$\begin{aligned} q_i(t+\Delta t) =& q_i(t) + \Delta t v_i(t) + A_i(t), && (2.14)\\ v_i(t+\Delta t) =& v_i(t) + \frac{1}{2}\Delta t \left[f_i(q_i(t+\Delta t)) + f_i(q_i(t))\right] && (2.15)\\ & -\frac{\gamma}{m_i}\Delta t v_i(t) + \sigma_i\sqrt{\Delta t}\xi_i(t) - \frac{\gamma}{m_i}A_i(t) \\ A_i(t) =& \frac{1}{2}\Delta t^2 (f(q(t)) - \frac{\gamma}{m_i}v_i(t)) + \sigma \Delta t^{3/2}\left(\frac{1}{2}\xi_i(t) + \frac{1}{2\sqrt(3)}\theta_i(t)\right). && (2.16) \end{aligned}$$

This second-order integrator introduces some common issues with numerical approximations in MD. First, the positions q_i and velocities v_i are updated at finite time points $t, t+\Delta t, \ldots, t+N_t\Delta t$, where $N_t\Delta t$ is the total duration of the simulation. Hence, the choice of Δt is fundamental, since large values would approximate the analytical solution with large errors, while small values would increase the total number of required timesteps for a given total simulated time interval, and, thus, increase the computational time. Second, the force fields $F_i(q_i(t)) = f_i(q_i(t))m_i$ have to be evaluated at two subsequent time steps t and $t+\Delta t$ to compute the velocity at timestep $t+\Delta t$, which implies that the force used to compute said velocity is an average of the forces acting on particle i at the two time points. Finally, specific for Langevin equations, appropriate random numbers ξ_i, θ_i have to be generated at each time point and for each particle, such that:

$$\langle \xi_i \xi_j \rangle = \langle \theta_i \theta_j \rangle = \delta_{ij}, \quad \langle \xi_i \theta_j \rangle = 0, \tag{2.17}$$

relations which follow from 2.13, as does the condition:

$$\sigma_i = \sqrt{\frac{k_B T \gamma}{m_i^2}}. \tag{2.18}$$

This set of equations have to be implemented as a computer software. Fortunately, some solid frameworks already exist and have been thoroughly tested. In fact, the simulations presented in chapter 4 have been performed using a custom version of the *Large-scale Atomic/Molecular Massively Parallel Simulator* (LAMMPS),[67] available at `http://lammps.sandia.gov`, which implements the algorithms outlined thus far.

This brief overview of MD techniques, although far from comprehensive of all issues necessary to set up a simulation, introduces the main concerns to address for the task: definition of the initial conditions and of the force-field. In fact, equations 2.14-2.16 require $q_i(0)$ and $v_i(0)$ to be initialised, and the evolution is determined by $f_i(q_i(t))$. Initial conditions have to be defined for each specific simulation (e.g. a Lennard-Jones gas might have all positions randomly generated and velocity either set to zero or drawn from a Maxwell-Boltzmann distribution), while force-fields will depend on the type of system being simulated. Our specific choices of $q_i(0)$ and $v_i(0)$ will be commented during the presentation of the results, while in the next section we will focus on the definition of the force-field for RBCs.

2.2 RBC force field

The typical biconcave shape of a human RBC, displayed in figure 2.2, is maintained by the combination of the outer lipid bilayer and the underlying spectrin network.[37] The resulting mechanical properties allow for large deformations, starting from the rest shape with diameter $D_0 = 7.8$ µm and squeezing into blood capillaries of diameter about 3 µm. The model developed by D. A. Fedosov, B. Caswell and G. E. Karniadakis[33] reflects these features by representing the membrane as a triangular mesh, with links mimicking the behaviour of the protein network. However, the real links in the spectrin network are replaced by effective springs, and the overall elastic parameters, e.g. the Young modulus, are used to adequately match the real mechanical properties of the RBC.

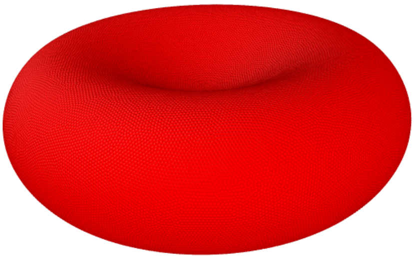

Figure 2.2: The typical shape of a Human RBC.

The analytical expression for the shape in figure 2.2 is given by:[68]

$$z = \pm D_0 \sqrt{1 - \frac{4\left(x^2+y^2\right)}{D_0^2}} \left(a_0 + a_1 \frac{x^2+y^2}{D_0^2} + a_2 \frac{\left(x^2+y^2\right)^2}{D_0^4} \right), \tag{2.19}$$

with $a_0 = 0.0518$, $a_1 = 2.0026$ and $a_2 = -4.491$. The area and volume of this shape are $A = 135$ µm^2 and $V = 94$ µm^2, respectively. The triangulated mesh is extracted from equation 2.19 using a Matlab (`https://www.mathworks.com/products/matlab.html`) package named DistMesh.[69] An example of such mesh is reported in figure 2.3. MD simulations of RBC meshes are performed applying equations 2.14-2.16 to each vertex of the triangles, with the force field described next.

The viscous component of the RBC dynamics was simulated in the original paper using Dissipative Particle Dynamics (DPD).[35,36] We chose to utilize Langevin equations instead, reducing the computational overhead related to the simulation of explicit water molecules, loosing, however, Galilean invariance, fundamental to correctly reproduce the hydrodynamic behaviour of RBC in blood stream. Such approximation holds well in our case, as we are not interested in the fluid dynamics of the RBC, but rather in the quasi-static behaviour close to adsorption.

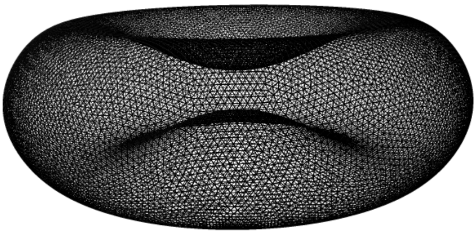

Figure 2.3: An example of triangulation of the RBC in figure 2.2. This particular mesh consists of 18830 vertices, connected via 56484 bonds.

The elastic potential employed is a combination of spring-like interactions, area and volume compression restraints and bending rigidity. The consistence of the choice was thoroughly checked against results from optical tweezers experiments,[33] and is deemed appropriate for our simulations. The first term in the potential is a two-point interaction, as illustrated in figure 2.4, and assumes the form:

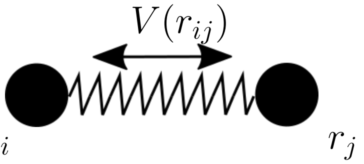

Figure 2.4: Example of two point interaction between vertices on the mesh.

$$V_{n_s}^{2p}(r_{ij}) = \frac{k_B T l_{max}}{4p} \frac{3x^2 - 2x^3}{1 - x} + \frac{k_p}{r_{ij}^m}. \tag{2.20}$$

In the equation l_{max} is the maximum spring extension, $x = r_{ij}/l_{max}$ is the instantaneous relative extension, with $x \in [0, 1)$, p is the persistence length, k_p and $m > 0$ are model parameters. The first term of equation 2.20 is the *Worm-like chain* potential, also reported in figure 2.5. The potential is purely compressive, therefore the second term is introduced to add local expansion.

The subsequent terms impede the collapse of the RBC on its center, pushing to preserve the original shape:

$$V_{area} = \frac{k_a (A - A_0^{tot})^2}{2 A_0^{tot}} + \sum_{j \in 1 \dots N_t} \frac{k_d (A_j - A_0)^2}{2 A_0}, \tag{2.21}$$

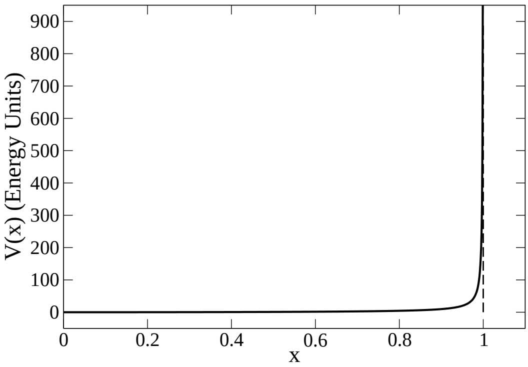

Figure 2.5: The *Worm-like chain* potential, with $k_B T l_{max}/4p = 1$, for simplicity. Units conventions are discussed in the forthcoming sections of this chapter.

$$V_{volume} = \frac{k_v (V - V_0^{tot})^2}{2V_0^{tot}}, \tag{2.22}$$

where A_0^{tot} is the total area of the RBC, A_0 is the equilibrium area of a single triangle, V_0 is the total volume of the cell, N_t is the total number of triangles, and k_a, k_d and k_v are model parameters. Figure 2.6 illustrates the meaning of the second term of equation 2.21. Finally, bending is taken into account by the last term:

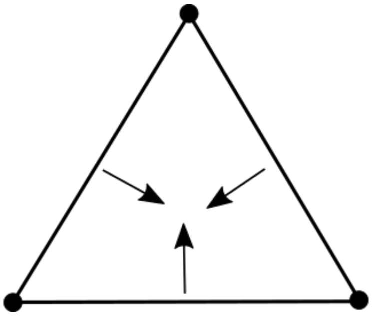

Figure 2.6: Illustrative example of the local area preservation term of equation 2.21. The bonds are pushed inwards if the current triangle area is larger than its equilibrium value, outwards in the opposite case.

$$V_{bending} = \sum_{j \in 1 \ldots N_s} k_b \left[1 - \cos(\theta_j - \theta_0)\right], \tag{2.23}$$

with θ_j the angle at the central bond of figure 2.7, and θ_0 the equilibrium value of said angle, related to the spontaneous curvature of the membrane. The sum runs over all bonds (springs) of the mesh. The complete expression for the potential of the triangulation can

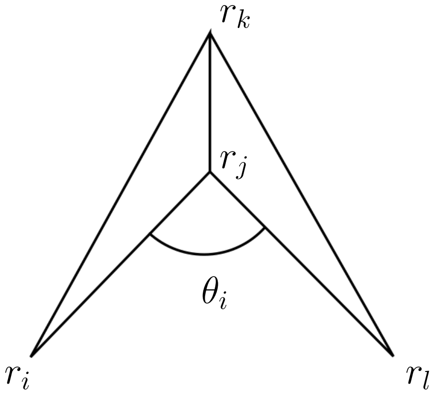

Figure 2.7: Definition of dihedral potential between the 4 vertices r_i, r_j, r_k and r_l.

thus be written as:

$$V(\mathbf{r}_i) = \sum_{n_s} V_{n_s}^{2p} + V_{area} + V_{volume} + V_{bending}, \tag{2.24}$$

to which it is necessary to add the inter-molecular potential (RBC-RBC, RBC-nanoparticles and RBC-surface):

$$V(r_{ij}) = 4\varepsilon \left(\left(\frac{\sigma}{r_{ij}} \right)^{12} - \left(\frac{\sigma}{r_{ij}} \right)^{6} \right) \tag{2.25}$$

which is represented by the classical Lennard-Jones Potential (figure 2.8). The definition of the form the potential is, thus, completely defined, and the forces, needed for Langevin Dynamics, can be computed as:

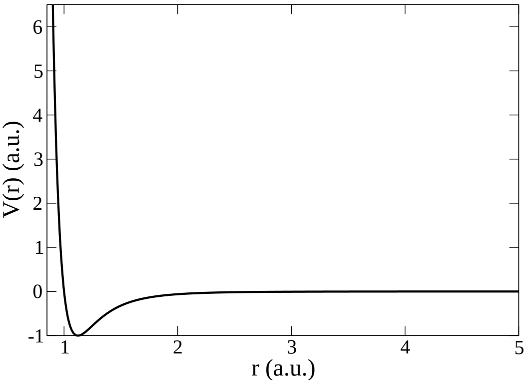

Figure 2.8: The classical Lennard-Jones potential, in units of $\sigma = \varepsilon = 1$.

$$\mathbf{f}_i = -\frac{\partial V(\{x_i\})}{\partial x_i}. \tag{2.26}$$

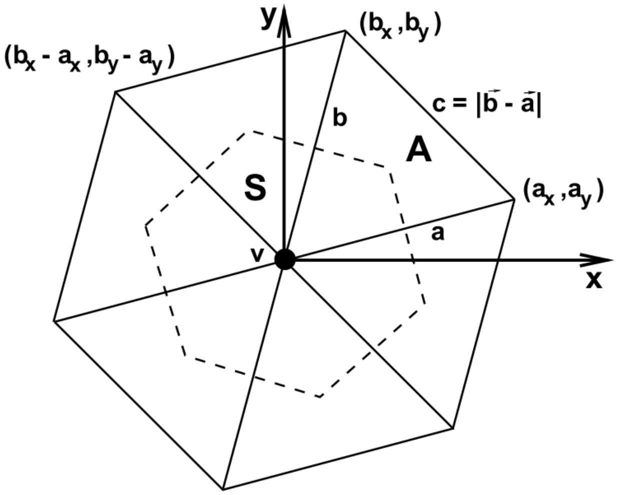

Figure 2.9: Hexagon constituted of 6 equilateral triangles, used to define the stress tensor of equation 2.27.

However, for the dynamics of simulated RBC to be predictive of the real cell mechanics, the microscopic parameters in the potential 2.24 have to be linked to the macroscopic parameters known from experiments.[70] Therefore, in the upcoming section, we are going to derive such linking relations.

2.3 Force field from real RBC mechanics

We start by considering an in-plane hexagon as in figure 2.9, formed by 6 equilateral triangles constituting the mesh of the membrane. From this figure we can calculate the contribution to the Cauchy stress tensor on vertex **v** from the potential in equation 2.24 using the virial theorem:[38, 71]

$$\begin{aligned}\tau_{\alpha\beta} = &-\frac{1}{2A}\left(\frac{f(a)}{a}a_\alpha a_\beta + \frac{f(b)}{b}b_\alpha b_\beta + \frac{f(c)}{c}(b_\alpha - a_\alpha)(b_\beta - a_\beta)\right) \\ &-\left(\frac{k_a(A_0^{tot} - N_t A)}{A_0^{tot}} + \frac{k_d(A_0 - A)}{A_0}\right)\delta_{\alpha\beta},\end{aligned} \tag{2.27}$$

where $S = 2A$ is the area inside the dashed line, A the area of a single triangle and $f(x)$ is the contribution to the force from $V_{n_s}^{2p}$. Since $A_0^{tot} = N_t A_0$, the second term can be written as $-(k_a + k_d)(A_0 - A)/A_0\delta_{\alpha\beta}$. Relation 2.27 allows to calculate the linear shear modulus by applying a small engineering shear strain Γ and computing $\mu_0 = \partial\tau_{\alpha\beta}/\partial\Gamma|_{\Gamma=0}$.[72, 73] This yields:

$$\mu_0 = \frac{\sqrt{3}k_B T}{4pl_{max}x_0}\left(\frac{x_0}{2(1-x_0)^3} - \frac{1}{4(1-x_0)^2} + \frac{1}{4}\right) + \frac{\sqrt{3}k_p(m+1)}{4l_0^{m+1}}, \tag{2.28}$$

with l_0 the equilibrium length of the spring and $x_0 = l_0/l_{max}$. Similarly, the area-compression modulus can be calculated from the in-plane pressure P (the system is 2 dimensional):

$$K = -\frac{\partial P}{\partial \log(A)}|_{A=A_0}, \tag{2.29}$$

where:

$$P = -\frac{1}{2}(\tau_{\alpha\alpha} + \tau_{\beta\beta}), \tag{2.30}$$

yielding, for the potential 2.24:

$$K = 2\mu_0 + k_a + k_d. \tag{2.31}$$

Finally, the Young modulus Y is defined as:

$$Y = \frac{4K\mu_0}{K + \mu_0}. \tag{2.32}$$

Generally, for a nearly incompressible sheet of bonds, as is the case of RBCs, $k_a + k_d \gg \mu_0$ and, thus, $K \gg \mu_0$.

Having outlined the links between microscopic and macroscopic elastic parameters, we are left with the parameters concerning bending. For this purpose, we consider the Helfrich Hamiltonian:[74]

$$\mathcal{H} = \frac{k_c}{2}\int_A (C_1 + C_2 - 2C_0)^2\, dA + k_g \int_A C_1 C_2 dA, \tag{2.33}$$

with k_c and k_g being the bending rigidities, C_1 and C_2 the local principal curvatures and C_0 the spontaneous curvature. The second term is generally omitted, since, on closed surfaces, it is constant, according to the Gauss-Bonnet theorem.[54] Assuming that the triangulation of the membrane is sufficiently smooth, we can treat small patches of the mesh as approximations of a spherical shell. Then, equation 2.33 reduces to:

$$\mathcal{H} = 8\pi k_c \left(1 - \frac{R}{R_0}\right)^2 \tag{2.34}$$

where $R = 1/C_1 = 1/C_2$ and $R_0 = 1/C_0$. The corresponding relation for the triangulated surface can be obtained from the construction in figure 2.10 and equation 2.23. This relation, up to second order in $(\theta - \theta_0)$, becomes:

$$V_{bending} = \frac{N_s k_b}{2}(\theta - \theta_0)^2 \tag{2.35}$$

Inspection of the figure leads to $\theta = a/(\sqrt{3}R)$, and analogously for θ_0. Moreover, $A^{tot} = 4\pi R \simeq N_t A_0 = \sqrt{3}N_t a^2/4 = \sqrt{3}N_s a^2/6$, or $a^2/R^2 = 8\pi\sqrt{3}/N_s$. Substituting in 2.35, yields:

$$V_{bending} = \frac{4\pi k_b}{\sqrt{3}}\left(1 - \frac{R}{R_0}\right)^2. \tag{2.36}$$

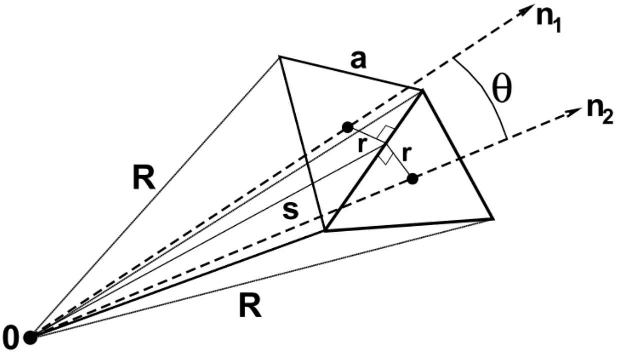

Figure 2.10: Illustration of the approximation of a spherical shell with a pair of triangles.

Finally, equating $\mathcal{H} = V_{bending}$ gives:

$$k_b = \frac{2}{\sqrt{3}} k_c, \quad \theta_0 = \arccos\left(\frac{\sqrt{3}N_s/2 - 5\pi}{\sqrt{3}N_s/2 - 3\pi}\right). \tag{2.37}$$

This last expression completes the set or relations we were seeking.

A last word before moving to the chapters presenting the results concerns the choice of units of measurement. The choice for the length scale is quite natural, being the size of RBCs, and other cells, in the order of a few µm. However, for other units, it is simpler, both for human comprehension and for computational accuracy, to work with numbers close to 1, e.g. ranging 10^{-3} to 10^3. Therefore, we define a reference quantity which allows simple conversion from "physical" units to model units. Labelling the former with P and the latter with M, we can use:

$$Y^P \frac{(k_B T)^P}{(D_0^P)^2} = Y^M \frac{(k_B T)^M}{(D_0^M)^2}, \tag{2.38}$$

where the Young modulus Y represents the reference quantity and the diameter D_0 is used to define length scale. From this relation, we can define the energy units for a given model:

$$(k_B T)^M = \frac{Y^p}{Y^M} \frac{(D_0^P)^2}{(D_0^M)^2} (k_B T)^P. \tag{2.39}$$

Analogously, we can define the model units for the time scale as:

$$t^M = \frac{D_0^P \eta^P Y_0^M}{D_0^M \eta^M Y_0^P} t^P, \tag{2.40}$$

where η is the dynamic viscosity and t is the unit of time. The relation between η and γ (equation 2.11), assuming the vertices to behave like small spheres of diameter d, is given by Stokes's law $\gamma = 3\pi d\eta$. The detailed choices made for the units will be discussed in the sections concerning the results.

Part II

Results

Chapter 3

Random Sequential Adsorption of proteins on Nanostructured Surfaces

The methods introduced in chapter 1 were used to produce the results described in the forthcoming sections. The problem of protein adsorption, specifically Human Serum Albumin (HSA) is treated with the RSA approach on model surfaces of *Psaltoda Claripennis* and Black Silicon (bSi), defined in terms of simple analytical functions. However, the dimensions of the original surfaces, as well as the size of the model proteins are chosen consistently. The details and motivations of our choices are explained in the first section concerning the setup of our computer experiments. After that, the actual results are shown and their interpretation is given, emphasising the most relevant conclusions for applications in biomedicine.

The first preliminary results from early simulations have been used to give a qualitative description of the protein adsorption process, and to accompany experimental observations.[75] The final quantitative conclusions outlined in this chapter are mostly in line with these observations, and have been submitted for publication.

3.1 Simulations setup

The choice to utilise HSA as the modelled protein is dictated mainly by it being the most abundant one in blood stream.[76] Although crystallographic data depicts HSA as heart-shaped,[43] in solution the excluded volume surrounding the protein screens its non-spherical shape. In fact, there is good agreement between Quartz Crystal Microbalance (QCM) experiments and models of spherical proteins[23] and, thus, HSA is generally treated as a sphere in theoretical modelling.[44] Hence, our simulations are performed on spheres of diameter $D = 7$ nm, which represents the typical size of HSA.[77]

The description of the surfaces is achieved by defining the nanostructures in the functional form:

$$f_i(x,y) = \begin{cases} H\exp\left(-\frac{(x-x_i)^2+(y-y_i)^2}{2v}\right) & \text{if } (x-x_i)^2+(y-y_i)^2 \le \frac{d_p^2}{4} \\ 0 & \text{otherwise} \end{cases}. \tag{3.1}$$

Here, $-d_p/2 < x < d_p/2$ and $-d_p/2 < y < d_p/2$, H denotes the height of the structures, $C_i = (x_i, y_i)$ is the center of the i-th peak, d_p is the peak-to-peak distance and $v = \left(\frac{W}{2}\right)^2 \frac{1}{2\log(2)}$ is the Gaussian variance, with W being the half height width. Choosing the C_i such that any two neighbouring peaks i and j satisfy either $C_j = C_i + (d_p, 0)$ or $C_j = C_i + (0, d_p)$, a periodic array of peaks is formed, mimicking the topology of nanopatterned surfaces. However, the quantities we compute are functions of θ, which is independent of the surface area, allowing us to use a single peak per simulation and reducing significantly the computational cost.

Two different sets of W and H values are employed to study the influence of the geometrical features on the final configuration of adsorption. The first one, defining model surfaces we denote as **Gaussian pillars**, consists of variations from the values $H = 200$ nm and $W = 80$ nm, while the second set, denoting **Gaussian spikes**, is initially given the values $H = 500$ nm and $W = 60$ nm. These quantities are somewhat reminiscent of the real surfaces *Psaltoda Claripennis* and bSi, although, for the sake of the modelling, we preferred a different denomination. Additionally, we explore the effect of concave structures, denoted as **Gaussian Holes**, and flat surface, mostly for comparison with previous works.

All simulations are repeated 1000 times, since the blocking function $B(\theta)$ and the jamming limit θ_∞ are defined as mean values of a statistically significant sample, as expressed by equation 1.10. This choices is deemed significant given that the standard deviation of the output data, used as statistical uncertainty, is unaltered for larger numbers of repetitions. Examples of final configuration of adsorbed HSA on a flat surface, on Gaussian pillars and spikes, and on a Gaussian Hole, are illustrated in figure 3.1.

Following the description of RSA on model surfaces, we employ the same approach on an Atomic Force Microscopy scan of a real bSi surface. AFM scans were performed at Swinburne University, using an Innova scanning probe microscope (Veeco, Bruker, Billerica, MA) in tapping mode, in air at at ambient conditions, using a silicon cantilever (Cont20A, Veeco Probes) with a spring constant of 0.9 N/m and a resonance frequency of ~ 20 kHz. The sample surfaces were first scanned with a 10 μm × 10 μm field of view to ensure even surface coverage and to avoid damaged areas (data not shown), before selecting 1 μm × 1 μm areas for scanning and analysis. Finally, for computer simulations, a 2.5 μm × 2.5 μm surface was extracted, due to memory performance hits for larger surfaces. A snapshot of the final state of these simulations is shown in figure 3.2.

3.2 RSA of HSA on model surfaces

The first observation concerns the behaviour of the Blocking function $B(\theta)$ for the four different geometries of figure 3.1. The plot in figure 3.3 shows that $B(\theta)$ is shifted towards larger values for Gaussian spikes with respect to the other surfaces, in particular for $\theta \to \theta_\infty$, and that the jamming limit is also increased. Given the arguments of sections 1.2

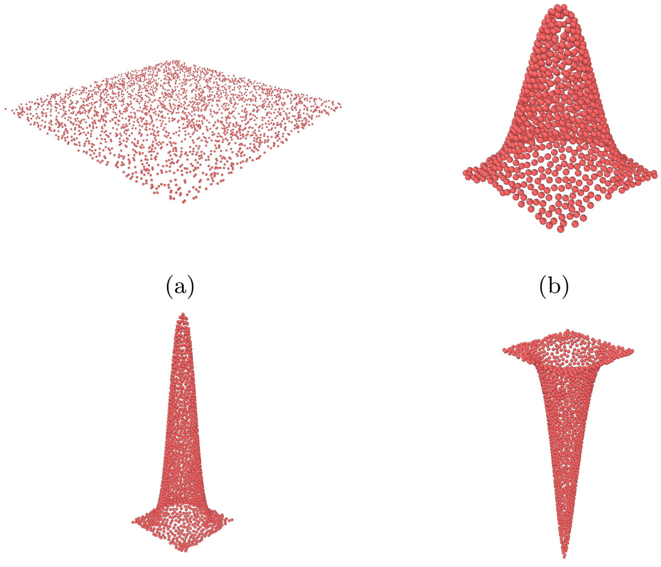

(a) (b)

(c) (d)

Figure 3.1: Final configuration for RSA simulations of four different surfaces: (a) Flat surface, (b) Gaussian spike with $W = 80$ nm and $H = 200$ nm (*Psaltoda claripennis* model), (c) Gaussian spike with $W = 60$ nm and $H = 500$ nm (BSi model) and (d) Gaussian "hole" with $W = 60$ nm and $H = -550$ nm. These snapshots have been obtained using OVITO.[78]

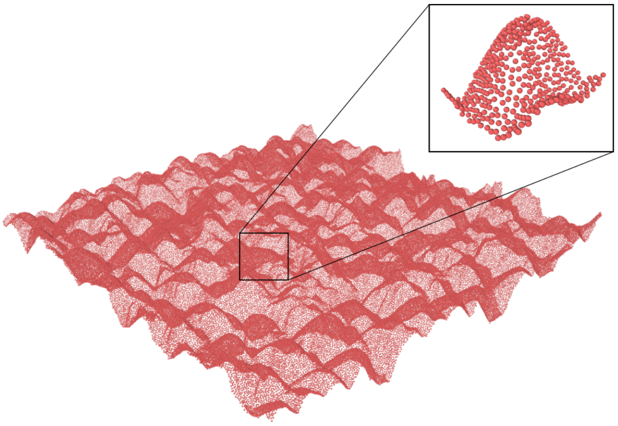

Figure 3.2: Final snapshot of an RSA simulation of albumin onto a BSi surface represented by an AFM scan.

and 1.3, this result is not surprising, since the Gaussian spikes have greater curvature at given height and are higher than the pillars. Analogously, the Gaussian Holes show lower occupancy than even the flat surface, effect caused by the negative curvature. Modifying the dimensions helps to further understand the role of length scales. Figure 3.4 illustrates the dependence of the blocking function on W and H for Gaussian pillars, while 3.5 depicts the same conclusions for Gaussian Spikes. Once more, the change of $B(\theta)$ is noticeable as the change of topology becomes more pronounced. In particular, the variability with the width for Gaussian spikes is quite large in figure 3.5a, due to larger curvatures associated to thinner spikes.

Consider the analysis of section 1.3, where we discussed the meaning of a Taylor expansion of the Blocking function with respect to θ. For small values of θ, only the first order term will be significant, and the behaviour for all types of surfaces is about the same. Hence, until overlap becomes relevant, surface geometry does not affect adsorption, as expected from $B(\theta) \sim 4\theta$. The curves start to spread apart when second and third order contributions become important. This effect occurs earlier for Gaussian Holes and flat surfaces, or for larger peaks, due to the larger effective area occupied by single spheres, as illustrated in figure 1.3. Therefore, the probability of adsorption, and, consequently, the Blocking function, is larger at fixed θ. The same argument leads to explain the larger values of the jamming limit θ, reported in table 3.1. The first row represents θ_∞ for flat surfaces resulting from our computations, while the value in the second row, from P. Schaaf and J. Talbot,[46] is used as reference to prove the consistence of our work with previous ones. The remaining entries outline a relation between strongly curved surface and the increase of the jamming limit. For instance, Gaussian spikes of height $H = 500$ nm and width $W = 40$ nm show in increase of $\Delta N = 9.5\%$ in the jamming limit, with the increase computed as:

$$\Delta N = \frac{N_s - N_f}{N_f} = \left(\frac{\theta_{\infty,s}}{\theta_{\infty,f}} - 1\right)\frac{A_s}{A_f}, \tag{3.2}$$

where N_i is the number of adsorbed proteins, A_i the area and s and f stay for spikes and flat, respectively. The relevance of this value of ΔN is even greater if we consider that $\Delta_N \simeq (0.9069/0.545 - 1) \simeq 0.6640$ is the same increase computed between hexagonal and random, and represents, thus, the largest expected value. The overall trend of increase of θ_∞ as a function of the curvature at half height $1/W$ is reported in figure 3.6.

Another property of experimental importance is the sequence of adsorption. For instance, in the work of D. H. K. Nguyen et al,[75] a colonisation of the valleys is observed at first, followed by adsorption at the top of the peaks. However, it is worth noticing that all the considerations have been made after equilibration, at different concentrations of HSA in solution. Therefore, the actual time dependence of the adsorption process is not transparent, but rather assumed based on the observed colonisation at increasing concentrations. Figure 3.7 displays the amount of proteins as a function of the vertical coordinates z, for both Gaussian pillars and spikes. Having generated the proteins with uniform probability over the actual manifold, the greater number of proteins at the bottom is a mere consequence of larger area availability. Although this is in line with the observations of D. H. K. Nguyen et al., their interpretation relies on more complex assumptions, since it is solely a consequence of greater surface availability.

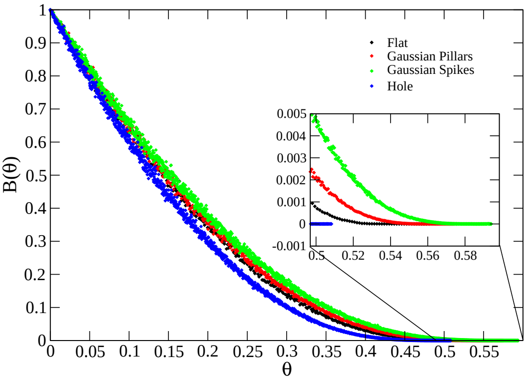

Figure 3.3: Blocking function $B(\theta)$ for: flat surface (black), Gaussian pillars (red), Gaussian spikes (green) and Gaussian hole (blue) defined by Equation (3.1). The inset highlights the ending points corresponding to θ_∞.

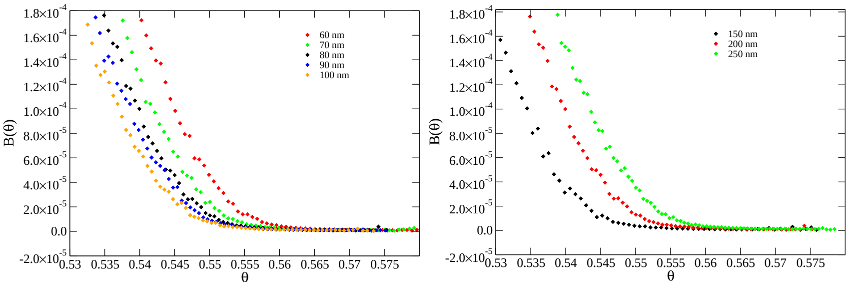

(a) (b)

Figure 3.4: Blocking function of pillars using (a) different widths at fixed height (200 nm), and (b) using different heights at fixed width (80 nm).

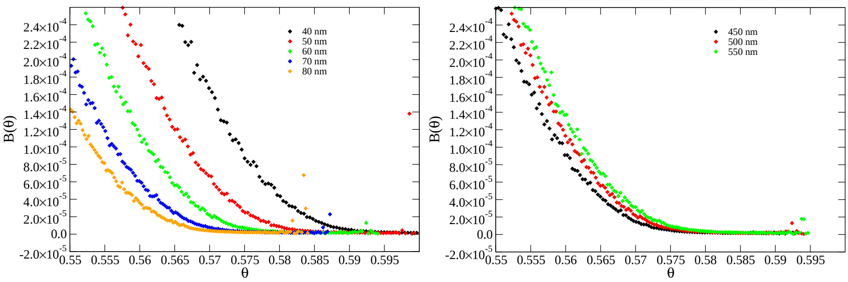

(a) (b)

Figure 3.5: Blocking function of spikes using (a) different widths at fixed height (500 nm), and (b) using different heights at fixed width (60 nm). The isolated points are due to fluctuations in the statistical sampling.

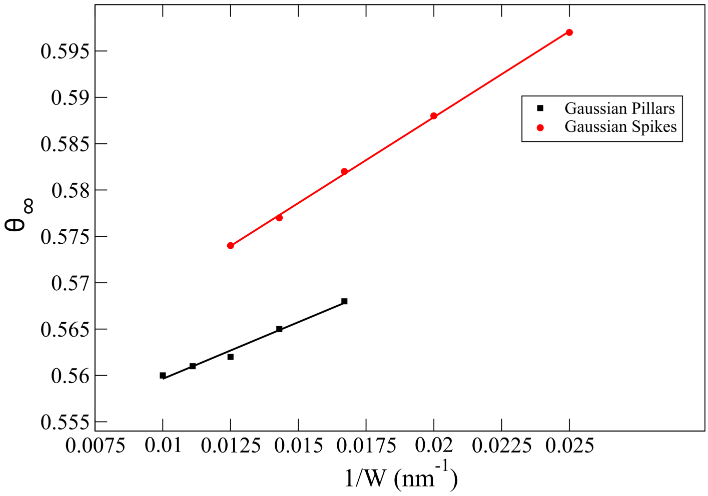

Figure 3.6: θ_∞ as a function of $1/W$ (i.e. the curvature) for both Gaussian Pillars (black) and Gaussian Spikes (red). The lines represent a linear fit, demonstrating a linear increase with increase of curvature.

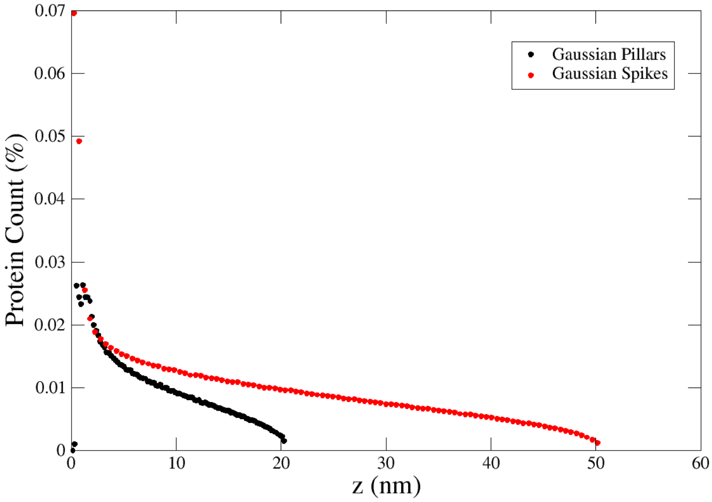

Figure 3.7: Vertical distribution of proteins for Gaussian Pillars with $W = 80$ nm and $H = 200$ nm, and for Gaussian Spikes with $W = 60$ nm and $H = 500$ nm. The number of proteins adsorbing on the bottom of the pillars is clearly much greater than that on the top of the pillars, a consequence of lower surface availability. The discontinuity in the left-hand side figure is a simple consequence of the definition of the shape, Eq. 3.1.

Table 3.1: Jamming limit θ_∞ for different geometries: flat surface, Gaussian pillars, Gaussian spikes and Gaussian holes. The values are obtained as the average of the coverage in the final state for each set of simulation. The error bars are estimated as standard deviation of each set. The values in the last column are the relative increase of number of adsorbed proteins with respect to the flat surface, $\Delta N = (N_s - N_f)/N_f$.

	H (nm)	W (nm)	A_s/A_f	θ_∞	$\Delta N(\%)$
Flat	-	-	1	0.545 ± 0.007	-
Flat (Schaaf *et. al.* [46])				0.547 ± 0.002	
Gaussian Pillars	150	80	1.7	0.558 ± 0.005	2.4
	200	60	1.9	0.568 ± 0.005	4.2
	200	70	2.0	0.565 ± 0.005	3.7
	200	80	2.1	0.562 ± 0.004	3.1
	200	90	2.2	0.561 ± 0.004	2.9
	200	100	2.2	0.560 ± 0.004	2.8
	250	80	2.5	0.566 ± 0.004	3.9
Gaussian Spikes	450	60	3.3	0.581 ± 0.004	6.6
	500	40	2.8	0.597 ± 0.004	9.5
	500	50	3.2	0.588 ± 0.003	7.9
	500	60	3.6	0.582 ± 0.003	6.8
	500	70	3.9	0.577 ± 0.003	5.9
	500	80	4.2	0.574 ± 0.003	5.3
	550	60	3.8	0.583 ± 0.003	7.0
Gaussian Hole	-550	60	3.8	0.499 ± 0.003	-8.4

The observations thus far on model surfaces can be used to interpret results on more complex topologies. The graph in figure 3.8 displays the blocking function of the surface in figure 3.2. The corresponding value of θ_∞ is 0.4576 ± 0.0003, smaller than the value for the Gaussian Hole. The interpretation is straightforward, given the analysis outlined above: the contribution to $B(\theta)$ from the hole-like structures, i.e. valleys, is greater than the contribution from the peaks. Therefore, the occupancy level is lower than the one obtained in the case of the flat surface. It is worth mentioning that the resolution of the AFM image introduces an experimental uncertainty that is greater than the theoretical error associated with our modeling approximations. Comparing the image presented in Fig. 3.2 to the figures reported by D. H. K. Nguyen,[75] it can be seen that the real pillars are steeper, while the AFM data introduces smoothing effects due to the cantilever jumping between the tips of the surface nanopillars. Nevertheless, our approach emphasizes the importance of considering the influence of topology in the process of protein adsorption, and how the geometry defines both the final configuration as well as the pattern of adsorption.

This last consideration concludes the analysis of the results obtained using RSA. However, further insight can be obtained by substituting the blocking functions for the various surfaces into equation 1.1. We describe the results of this approach in the following section, and conclude this chapter with a comparison of RSA with the excessively used Langmuir model.

3.3 The timescale of HSA adsorption onto nanostructured surfaces

An interesting question that arises in practical adsorption experiments concerns the time required for proteins to adsorb onto a substrate surface. We use the fourth-order Runge-Kutta method[79, 80] to numerically solve equation 1.1 for albumin taken at the concentration corresponding to that in blood plasma ($n = 5.3 \cdot 10^{-4}$mol/L) and an arbitrary lower concentration ($n = 1.06 \cdot 10^{-5}$mol/L) leads to the solutions shown in figures 3.9 and 3.10.

The curves rapidly reach plateau values, which are dependent on the jamming limit. Saturation of the surface is reached in tens of seconds at low protein concentration, and a few seconds at the higher protein concentration corresponding to that found in blood plasma. Since the desorption constant $k_d = 5.78 \cdot 10^{-4}$ s^{-1} is small compared to the adsorption $k_a = 10^4$ Lmol^{-1}s^{-1}, the plateau values are very close to those reported in Table 3.1, which is in line with the assumption that irreversible (or almost irreversible) adsorption is taking place.

Note however, that our model does not take into account the diffusion time τ_D required by the proteins to reach the surface. For the aforementioned approximations to hold, this time scale needs to be smaller than the time scale of adsorption τ_a. The diffusion time can be estimated as $\tau_D = h^2/D$, where D is the diffusion coefficient. For albumin, this assumes the value[40] $D_{dif} = 2.15 \cdot 10^{-11}$ m^2/s, and h is the typical length scale of the interaction between proteins and surface. Diffusion depends on the geometry and, thus, the quantity h will be, in general, a function of the surface structure. For an estimate value of h, however, we can consider a volume hA close to the surface, where the density of non-adsorbed proteins is n. Then, equating the amount of protein adsorbed to the surface to the amount still in this interaction range, we obtain:

$$\frac{A}{\sigma} = nhA \tag{3.3}$$

Diffusion is negligible if:

$$\tau_a \gg \tau_D = \frac{1}{n^2 \sigma^2 D}, \tag{3.4}$$

yielding, for the two concentrations in figures 3.9-3.10, $\tau_D \simeq 0.8$ s and $\tau_D \simeq 3.1 \cdot 10^{-4}$ s. Thus, for albumin at the concentration found in blood, the timescale of adsorption is a good approximation of the overall time required to cover the surface with the protein. At lower concentrations, an important contribution to the time of adsorption comes from the time required for the proteins to diffuse to the surface. Therefore, a different approach, coupling the diffusion equation to the RSA model, like the generalized RSA model,[40] would lead to the calculation of more accurate timescales in the case of low protein concentrations. In

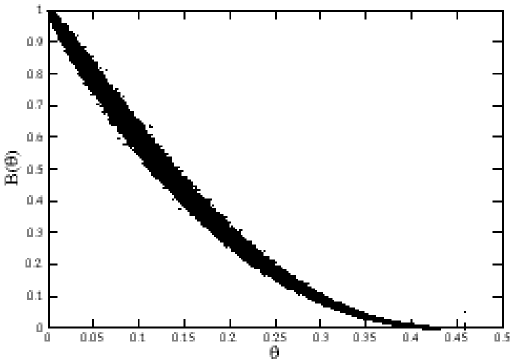

Figure 3.8: Blocking function of albumin adsorption on the AFM scan of the real BSi surface.

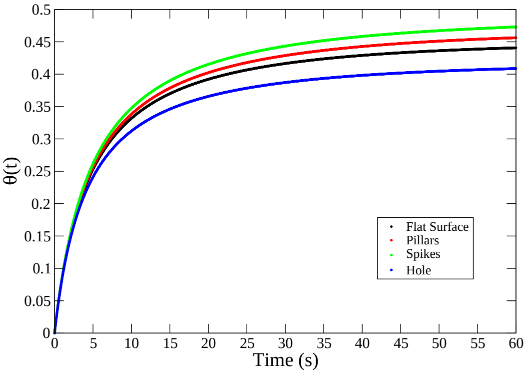

Figure 3.9: Coverage as a function of time for the four surfaces investigated ($n = 1.06 \cdot 10^{-5}$mol/L).

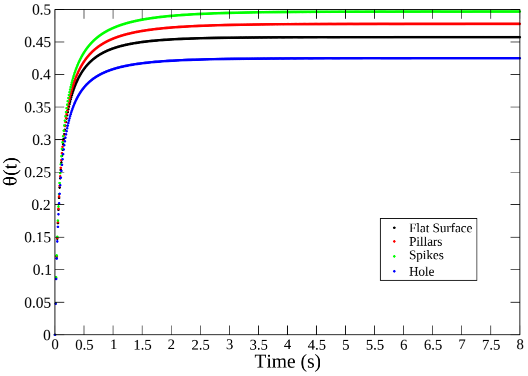

Figure 3.10: Coverage as a function of time for the four surfaces investigated ($n = 5.3 \cdot 10^{-4}$mol/L).

the case of albumin adsorption at realistic concentration values, however, the simple RSA model allows good estimates of typical timescales to be determined.

3.4 Comparison of Langmuir and RSA approaches

Since Langmuir adsorption isotherms are widely used for modelling experimental data, we compared the results obtained by the Langmuir model with those obtained using the RSA model. Langmuir isotherms were obtained using equation 1.2, using the typical value $K_{eq} = 1.73 \times 10^7$ L/mol of the adsorption constant, which is valid for albumin.[26] The saturation occupancy θ_∞ was estimated as an upper boundary, assuming hexagonal packing. For a flat surface, this becomes $\theta_\infty = \frac{\pi}{4} \simeq 0.9069$ and for a nanostructured surface made of cylindrical pillars, $\theta_\infty = 0.92$. These are estimated values for the purpose of comparing the Langmuir and RSA models.

The different saturation values θ_∞ obtained via the Langmuir adsorption with respect to the jamming limits in Table 3.1 provides an insight into the departure expected from such an approach to an irreversible adsorption process. Even if it is assumed that the Langmuir saturation value matches that of the RSA model, fitting the data using the Langmuir model would be incorrect, as shown in figure 3.11. The plot shows a steady solution of equation 1.1 for several values of concentration n, as is common in the Langmuir approach. While the coefficients k_a and k_d used to derive the two curves are set to the same value in both cases, the Langmuir isotherm reached saturation at a lower concentration than that obtained using the RSA model. Conversely, if the Langmuir model was used to fit the RSA data, the resulting adsorption and desorption constants would likely lead to wrong interpretations of adsorption behaviour being made.[26]

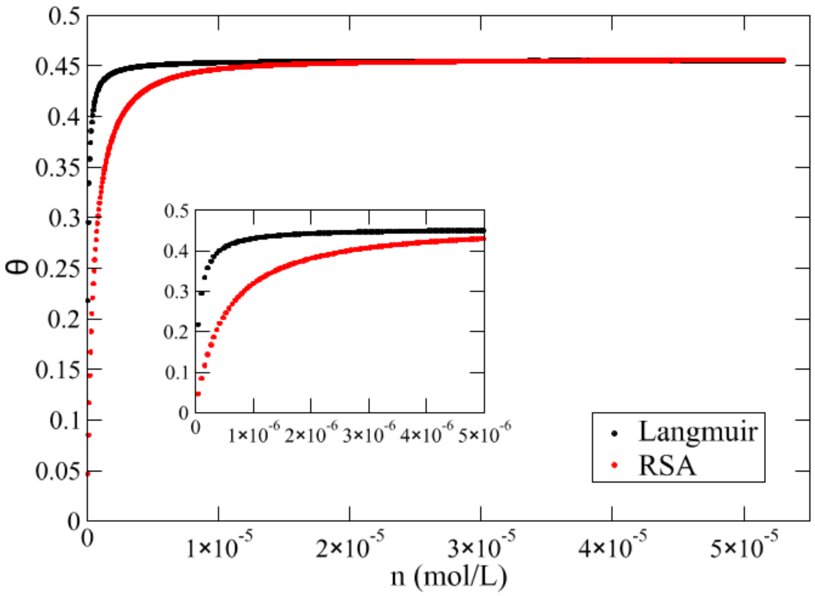

Figure 3.11: RSA isotherm (red) in comparison with the Langmuir isotherm (black) for spherical proteins adsorbing onto a flat surface.

Chapter 4

Strain-stress analysis of deformed RBCs

The results of the second part of our project are outlined below. We discuss the effect of mechanical deformations on the viscoelastic membrane of Red Blood Cells (RBCs), to understand how rupture occurs on antimicrobial surfaces, despite their large deformability in blood vessels.

A major drawback of the computer models we describe in the following sections is the need for discretisation to numerical solve the equations of motion. We introduced the problem in chapter 2, where we presented the RBC membrane as a triangulated manifold, with each vertex moving as an MD particle. However, we did not mention that the surface of a single triangle of the mesh is empty, and, in principle, external particles could move through it, creating an artifact related to the approximation used. The issue is fixed by an appropriate choice of all σ_i in equation 2.25, where the index runs over all possible pair types in the simulation. For instance, if the vertices have diameter d_v and the external particle d_p, $\sigma_{pp} = d_p$ and $\sigma_{pv} = (d_p + d_v)/2$, then the condition for impermeability is (see figure 4.1):

$$r_{vv} < \sqrt{3}\sigma_{pv}, \tag{4.1}$$

where r_{vv} is the center to center distance between two vertices. In practice, r_{vv} is varying due to the dynamics of the RBC, and condition 4.1 is required to be satisfied at all time steps. Eventually, if this is not the case over the duration of simulation, a finer mesh can be employed. However, for nanopatterned surfaces, as the erythrocyte adheres to the surface, r_{vv} will inevitably increase to the point where the condition is no longer valid, and the peak will enter the membrane.

Mainly for these reasons, we started the simulations analysing the deformability of RBCs upon adsorption of nanoparticles (NPs) on the cells, as this problem is topologically equivalent, but condition 4.1 can be maintained at all time steps. Obviously, this type of systems has its own experimental importance,[81] and we will discuss our conclusions with either cases in mind.

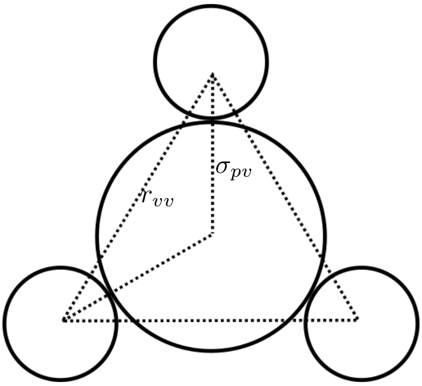

Figure 4.1: Scheme representing the limiting condition for a triangle to be impermeable, without explicitly defining it as solid.

4.1 Simulations of Nano-particle adsorption on RBCs

The simulated systems in this section consist of an RBC and a varying number N_p of NPs of diameter $d_p = 200$ nm. The NPs are initially placed in the neighbourhood of the cell, to reduce the computational cost. For the first set of simulations, this placement is chosen at random, giving a situation as in figure 4.2, where the images illustrate the initial configuration ($t = 0$) and the configuration after 500 timesteps.

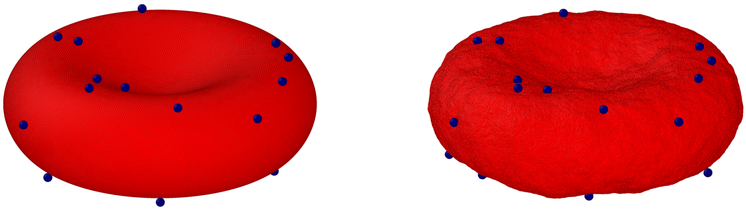

Figure 4.2: A system consisting of an RBC and 25 Nps distributed at random around the cell. The figures depict the system at the beginning of the simulation and after 500 timesteps.

At this stage, it is compulsory to highlight some important features of our simulations. First, the RBC is cleary at its minimum shape at the start of the calculations, which, however, does not correspond to its thermodynamic equilibrium at body temperature. Therefore, before "switching on" the interaction potentials between NPs and the RBC, the latter is left to relax towards the target temperature using the thermostat (equation 2.11). Only following equilibration are the inter-body forces activated, driving the whole system to its new thermodynamic steady state.

The variations of the total area and the total volume of the RBC are used to quantify the deformation of the membrane. Figure 4.3 shows the outcome of the first set of such simulations for 1, 2, 3, 5, 10, 25, 50, 75 and 100 Nps adsorbing to an RBC. The plots show

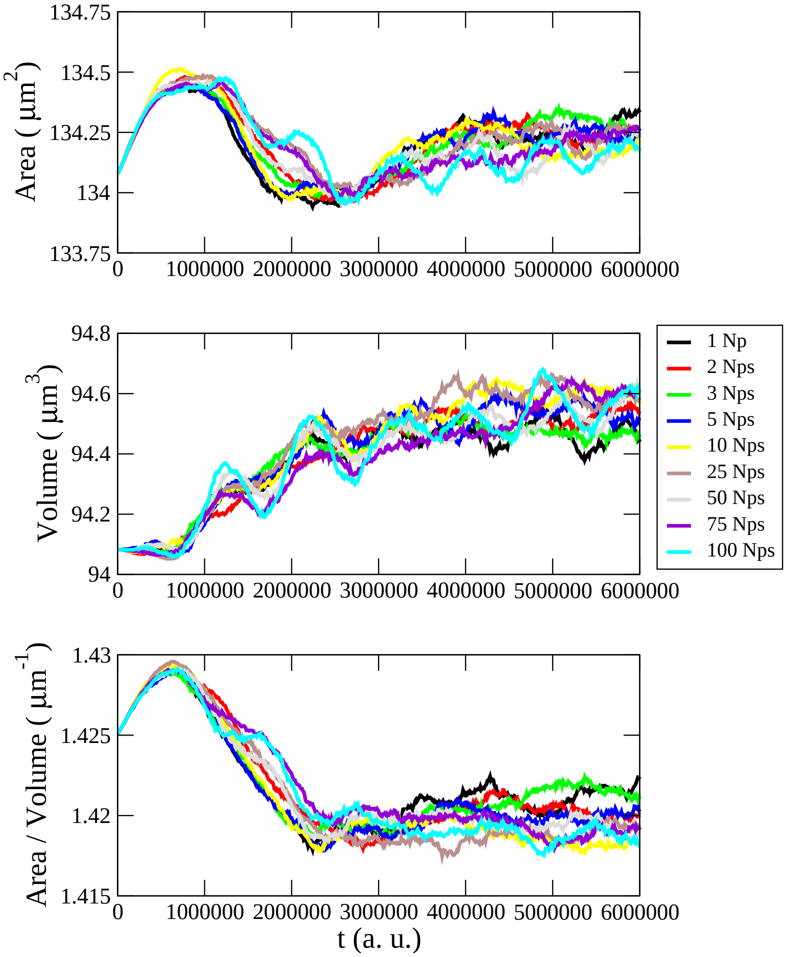

Figure 4.3: Graphs displaying, from top to bottom, Area, Volume and Area to Volume ratio as a function of time for a RBC adsorbing 1, 2, 3, 5, 10, 25, 50, 75 and 100 Nps of diameter 200 nm (see legend). The final quantities are almost indifferent to the amount of particles sticking to the cell.

that increasing the number of Nps does not affect relevantly the shape of the cell, with the area and volume changing, from 1 to 100 Nps, by less than 0.2%. Note that the time steps are reported in *arbitrary units*, whose actual definition is worth a few observations.

All the simulations use µm as units of length, making the definition of area and volume units straightforward. For energy units, we apply relation 2.39 to impose $(k_BT)^M = 1$, which decreases the numerical rounding errors in the computations, and which can be obtained from:

$$Y^M = Y^P \left(\frac{D_0^P}{D_0^M}\right)^2 \frac{(k_BT)^P}{(k_BT)^M} \simeq (18.9 \cdot 10^{-9})(10^9)(4.3 \cdot 10^{-21}) \simeq 81.3 \cdot 10^{-21} \text{model units}, \tag{4.2}$$

where as physical parameters we have used the International System of Units (SI), $T = 310K$ is the body temperature and $Y^P = 18.9$ µN/m.[33] Analogously we define the time step from equation 2.40:

$$t^M \simeq (10^9)\frac{6.9 \cdot 10^{-4}}{3.2}\frac{81.3 \cdot 10^{-21}}{18.9 \cdot 10^{-9}} s \simeq 9.3 \cdot 10^{-7} s \simeq \text{µs}, \tag{4.3}$$

where s stays for seconds, $6.9 \cdot 10^{-4} Pa \cdot s$ is the dynamic viscosity of water at 310 K and 3.2 is an arbitrary viscosity value in model units. This value, as well as the size of the time step $\Delta t = 10^{-6} t^M$ are chosen after some trial and error: greater values of Δt easily lead to instabilities, while greater value of η will slow down the simulations to a point where no motion is observed. Consequently, the total duration of a simulation is in the order of $6 \cdot 10^6 \Delta t = 6$ µs.

Having clarified our choice of units, we continued our work by changing, more precisely increasing, the size of the NPs. As already mentioned, we expect dimensions of the structures adsorbing to RBCs to have a leading role, in addition to a greater amount, e.g. more peaks. Figure 4.4 depicts the same snapshot as the right-hand side of figure 4.2, for NPs of diameter $d_p = 400$ nm. For this second set of simulations, only two different amounts have been chosen, 25 and 50, as smaller variations did not give much insight in the former computations. The area and volume deformations of this second case are reported in figure 4.5. Although the area increase is still of the order of 0.17%, the volume increase starts to be slightly larger, about 0.32%, which does not represent a significant variation,

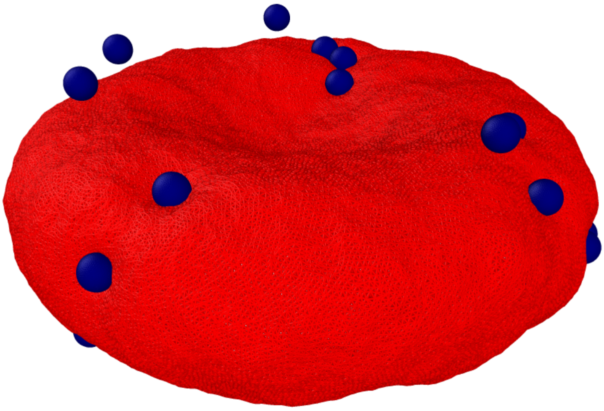

Figure 4.4: Snapshot of a simulation using 25 NPs of size 400 nm, at $t = 500\Delta t$.

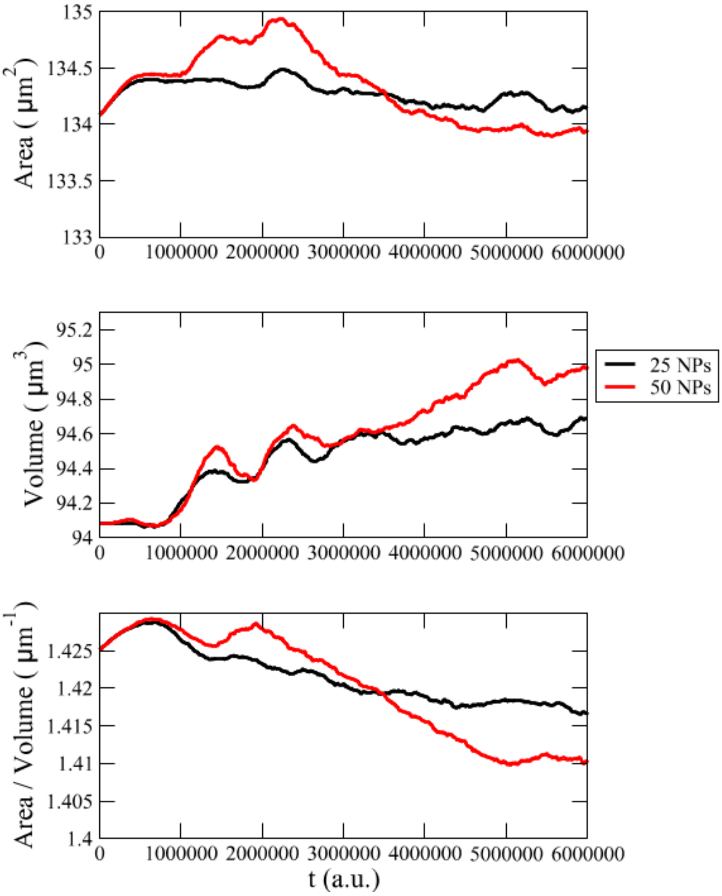

Figure 4.5: Area, Volume and Area to Volume ratio as a function of time, for 25 and 50 NPs of diameter 400 nm.

but suggests a trend with the dimensions of the interacting structures. Notice also that the area to volume ratio is decreasing: this behaviour reflects the tendency of the RBC to deform towards a more spherical shape, since the expected ratio for a sphere of diameter $D_0 = 7.82$ µm is 0.767 µm.

Another contribution which could enhance the deformations of RBCs is given by co-operative effects. Thus far we have spread the NPs at random close to the surface of the RBCs, and, locally, only one, or at times two, NPs contribute to the deformations. Consequently, the elasticity of the cell membrane might be enough to relax the strains with little effect on the overall shape.

Figure 4.6 shows an example of a configuration where 19 NPs are placed symmetrically at the center of the upper side of the RBC membrane. Similar simulations have been performed for 1, 2, 19 and 55 NPs, with the latter two choices dictated solely by symmetry.

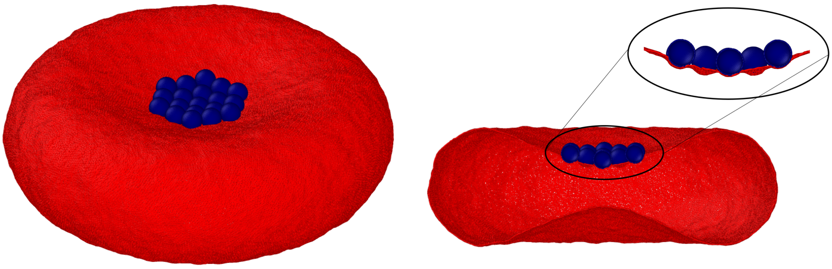

Figure 4.6: Configuration at timestep $t = 500\Delta t$ of a system with 19 NPs all placed at the center of the top side of the RBC. On the right-hand side the central section is displayed, to show the local deformations.

The results of these computations are displayed in figure 4.7. Comparing to figure 4.5, we observe less fluctuations in the final surface area, but a greater increase in volume ($\simeq 1.09\%$), and, consequently, greater decrease towards the sphere area-volume ratio.

We can deduce from these considerations that the size of the structures does affect the overall shape of the visco-elastic sheet of springs describing the RBC, but that cooperative effects are more relevant. The cell membrane is able to accommodate a large number of small local deformations easier than a single, large deformation occurring only on one side of the membrane. Therefore, we expect a surface such as bSi, pushing only on one side, to enhance this effect even more.

Particular emphasis is devoted to the volume increase observed in the simulations. This phenomenon indicates that the RBC, despite its ability to conserve area, begins to blow, eventually reaching a point where it can not accommodate the deformations any more, and, consequently, rupture is observed. However, our model does not predict breaking bonds, and eventual rupture must be inferred from comparison with empirical data.

A final word is due at this point concerning the choice of ε, the parameter determining the strength of the Lennard-Jones interaction, equation 2.25. We did not discuss its value thus far because the variation is not significant over the range of physical values (a few k_BTs). In fact, figure 4.8 displays the area, volume and area to volume ratio obtained for a system with 1 NP of size 400 nm placed at the center of the RBC, with $\varepsilon = 2.5k_BT$ and $\varepsilon = 10k_BT$. No noticeable effect is deducible, confirming the statement.

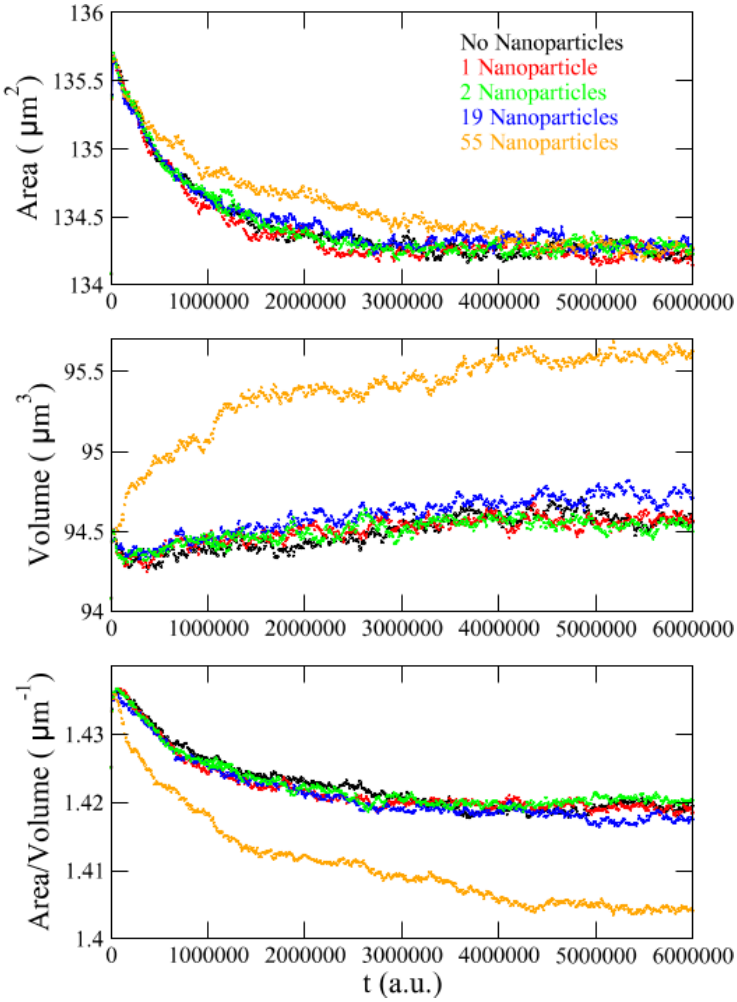

Figure 4.7: Area, Volume and Area to Volume ratio for a system with no, 1, 2, 19 and 55 NPs, placed symmetrically around the central point on the top side of the RBC.

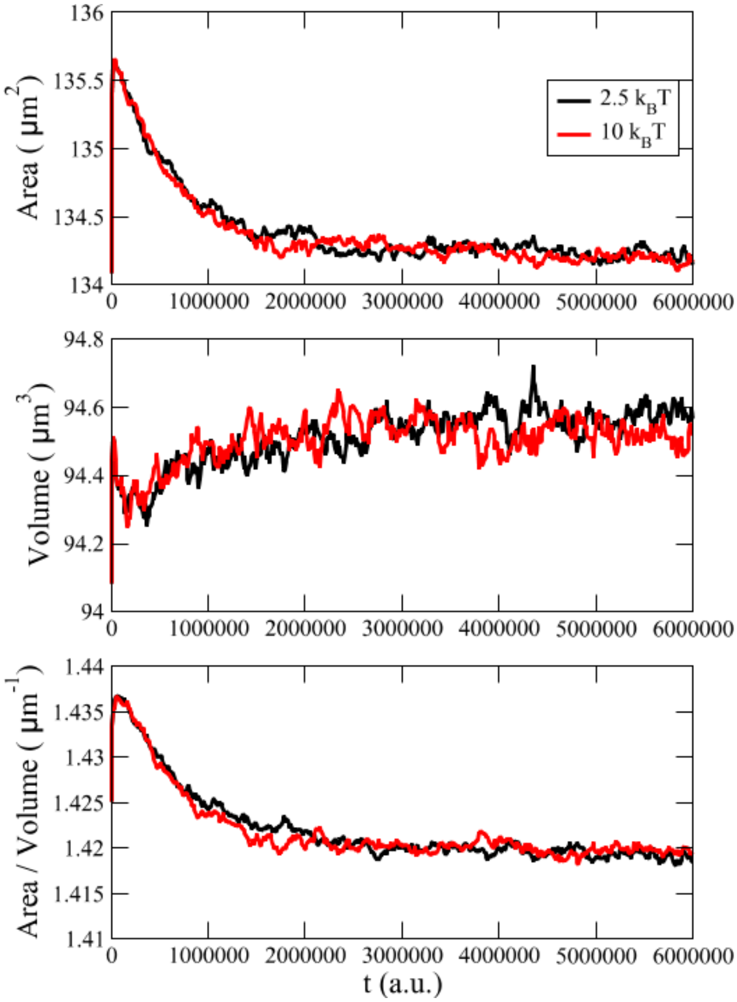

Figure 4.8: Area, Volume and Area to Volume ratio for a system with 1 NP on the RBC, at $\varepsilon = 2.5k_BT$ and $\varepsilon = 10k_BT$.

Conclusions

This work describes the approaches to two different problems related to biomaterials, which have been recently of major interest in literature. The first one concerns protein adsorption on nanostructured surfaces, in particular HSA, which is the first protein colonising a foreign object entering blood. The second problem is represented by the mechanical rupture of RBCs on said surfaces, an undesired collateral effect of these antimicrobial topologies.

Protein adsorption has been studied using RSA, an approach which implicitly assumes irreversibility, making it an optimal candidate for this type of problem. We demonstrate the importance of curvature effects on the amount of adsorbed particles, and additionally determine estimations for the time scales of adsorption, of the order of a few seconds. We confirm the trend observed by former experiments,[48] that the total amount of adsorbate at saturation is larger than the quantity expected by a mere proportionality with the surface area, and we also explain the sequence for HSA adsorption described in the experiments of D. H. K. Nguyen et al.[75] Finally, we stress once more the importance of abandoning the Langmuir adsorption approach, still excessively used to predict protein isotherms, despite its inherently inconsistent assumptions.[26]

RBC has been investigate using coarse-grained MD, specifically Langevin equations, and interesting results on shape deformations upon NPs adsorption have been found. Particularly, we demonstrated that the membrane is generally capable of accommodating area deformations, at the cost of increasing its volume. This effect can lead to excessive stress and, eventually, to rupture.

An important observation valid for both cases concerns size effects. The purely geometric results of chapter 3 and the physical simulations of chapter 4 highlight the relevance of the dimensions mismatch between adsorbent and adsorbate, being it a NP adsorbing to a RBC or HSA adsorbing to bSi. This apparently straightforward consideration is often overlooked in biological systems, where more complex explanations are sought. Our work moves somewhat into the opposite direction, nevertheless capable of deducing some relevant features of otherwise very complex systems.

Bibliography

[1] B. D. Ratner and S. J. Bryant. *Biomaterials: Where We Have Been and Where We Are Going.* Annu. Rev. Biomed. Eng., **6(1)**:41–75 (2004).

[2] J. Yin and S. Luan. *Opportunities and challenges for the development of polymer-based biomaterials and medical devices.* Regen. Biomater., **3(2)**:129–135 (2016).

[3] B. D. Ratner, A. S. Hoffman and F. J. Schoen. *Biomaterials science: An introduction to materials in medicine.* 2013. Academic Press, third edit edition (2013).

[4] N. Patel and P. Gohil. *A review on biomaterials: scope, applications & human anatomy significance.* Int. J. Emerg. Technol. Adv. Eng., **2(4)**:91–101 (2012).

[5] K.-H. Jeong. *Biologically Inspired Artificial Compound Eyes.* Science (80-.)., **312(5773)**:557–561 (2006).

[6] I. Kurtz and J. Schiffman. *Current and Emerging Approaches to Engineer Antibacterial and Antifouling Electrospun Nanofibers.* Mater. 2018, Vol. 11, Page 1059, **11(7)**:1059 (2018).

[7] H. F. Hildebrand. *Biomaterials a history of 7000 years.* BioNanoMaterials, **14(3-4)**:119–133 (2013).

[8] N. Huebsch and D. J. Mooney. *Inspiration and application in the evolution of biomaterials.* Nature, **462(7272)**:426–432 (2009).

[9] D. F. Williams. *Definitions in biomaterials : proceedings of a consensus conference of the European Society for Biomaterials, Chester, England, March 3-5, 1986.* Elsevier (1987).

[10] Magnus S. Ågren. *Wound Healing Biomaterials Volume 2: Functional Biomaterials.* Woodhead Publishing (2016).

[11] J. Hasan, R. J. Crawford and E. P. Ivanova. *Antibacterial surfaces: The quest for a new generation of biomaterials.* Trends Biotechnol., **31(5)**:295–304 (2013).

[12] A. M. Kraigsley and S. E. Finkel. *Adaptive evolution in single species bacterial biofilms.* FEMS Microbiol. Lett., **293(1)**:135–140 (2009).

[13] A. T. Sidambe. *Biocompatibility of Advanced Manufactured Titanium Implants-A Review.* Mater. (Basel, Switzerland), **7(12)**:8168–8188 (2014).

[14] W. Att, N. Hori, M. Takeuchi et al. *Time-dependent degradation of titanium osteoconductivity: An implication of biological aging of implant materials.* Biomaterials, **30(29)**:5352–5363 (2009).

[15] K. Bazaka, M. V. Jacob, R. J. Crawford et al. *Efficient surface modification of biomaterial to prevent biofilm formation and the attachment of microorganisms.* Appl. Microbiol. Biotechnol., **95(2)**:299–311 (2012).

[16] E. P. Ivanova, J. Hasan, H. K. Webb et al. *Bactericidal activity of black silicon.* Nat. Commun., **4**:2838 (2013).

[17] X. Liu, P. R. Coxon, M. Peters et al. *Black silicon: fabrication methods, properties and solar energy applications.* Energy Environ. Sci., **7(10)**:3223–3263 (2014).

[18] K. Liu and L. Jiang. *Bio-inspired design of multiscale structures for function integration.* Nano Today, **6(2)**:155–175 (2011).

[19] E. P. Ivanova, J. Hasan, H. K. Webb et al. *Natural bactericidal surfaces: Mechanical rupture of pseudomonas aeruginosa cells by cicada wings.* Small, **8(16)**:2489–2494 (2012).

[20] S. Pogodin, J. Hasan, V. a. Baulin et al. *Biophysical model of bacterial cell interactions with nanopatterned cicada wing surfaces.* Biophys. J., **104(4)**:835–840 (2013).

[21] X. Li. *Bactericidal mechanism of nanopatterned surfaces.* Phys. Chem. Chem. Phys., **18(2)**:1311–1316 (2016).

[22] Z. Adamczyk. *Particles at Interfaces Interactions, Deposition, Structure.* Interface Sci. Technol. (2006).

[23] E. A. Vogler. *Protein adsorption in three dimensions.* Biomaterials, **33(5)**:1201–1237 (2012).

[24] L. Vroman. *The life of an artificial device in contact with blood: initial events and their effect on its final state.* Bull. N. Y. Acad. Med., **64(4)**:352–357 (1988).

[25] I. Langmuir. *The adsorption of gases on plane surfaces of glass, mica and platinum.* J. Am. Chem. Soc., **40(9)**:1361–1403 (1918).

[26] R. A. Latour. *The Langmuir isotherm: A commonly applied but misleading approach for the analysis of protein adsorption behavior.* J. Biomed. Mater. Res. - Part A, **103(3)**:949–958 (2015).

[27] J. Talbot, G. Tarjus, P. R. Van Tassel et al. *From car parking to protein adsorption: An overview of sequential adsorption processes.* Colloids Surfaces A Physicochem. Eng. Asp., **165(1-3)**:287–324 (2000).

[28] J. Feder. *Random Sequential Adsorption.* J. Theor. Biol, **87**:237–254 (1980).

[29] Z. Adamczyk, J. Barbasz and M. Ciesla. *Mechanisms of Fibrinogen Adsorption at Solid Substrates.* Langmuir, **27(11)**:6868–6878 (2011).

[30] B. Widom. *Random Sequential Addition of Hard Spheres to a Volume.* J. Chem. Phys., **44(10)**:3888–3894 (1966).

[31] V. T. H. Pham, V. K. Truong, D. E. Mainwaring et al. *Nanotopography as a trigger for the microscale, autogenous and passive lysis of erythrocytes.* J. Mater. Chem. B, **2(19)**:2819 (2014).

[32] E. A. Evans and R. Skalak. *Mechanics and Thermodynamics of Biomembranes.* Taylor & Francis Group (1980).

[33] D. A. Fedosov, B. Caswell and G. E. Karniadakis. *Systematic coarse-graining of spectrin-level red blood cell models.* Comput. Methods Appl. Mech. Eng., **199(29-32)**:1937–1948 (2010).

[34] D. A. Fedosov, B. Caswell and G. E. Karniadakis. *A multiscale red blood cell model with accurate mechanics, rheology, and dynamics.* Biophys. J., **98(10)**:2215–2225 (2010).

[35] P. J. Hoogerbrugge and J. M. V. a. Koelman. *Simulating Microscopic Hydrodynamic Phenomena with Dissipative Particle Dynamics.* Europhys. Lett., **19(3)**:155–160 (2007).

[36] R. D. Groot and P. B. Warren. *Dissipative particle dynamics: Bridging the gap between atomistic and mesoscopic simulation.* J. Chem. Phys., **107(11)**:4423 (1997).

[37] Y. C. Fung. *Biomechanics : mechanical properties of living tissues.* Springer-Verlag (1993).

[38] M. E. Tuckerman. *Statistical mechanics : theory and molecular simulation.* Oxford University Press (2010).

[39] J. J. Gray. *The interaction of proteins with solid surfaces.* Curr. Opin. Struct. Biol., **14**:110–115 (2004).

[40] Z. Adamczyk. *Particles at Interfaces: Interactions, Deposition, Structure.* Elsevier (2006).

[41] Z. Adamczyk, B. Senger, J.-C. Voegel et al. *Irreversible adsorption/deposition kinetics: A generalized approach.* J. Chem. Phys., **110(6)**:3118 (1999).

[42] R. A. Latour. *Molecular simulation of protein-surface interactions: Benefits, problems, solutions, and future directions " Review. . . .* Biointerphases, **3(3)**:FC2–FC12 (2008).

[43] S. Sugio, A. Kashima, S. Mochizuki et al. *Crystal structure of human serum albumin at 2.5 Å resolution.* Protein Eng. Des. Sel., **12(6)**:439–446 (1999).

[44] P. Vilaseca, K. A. Dawson and G. Franzese. *Understanding and modulating the competitive surface-adsorption of proteins through coarse-grained molecular dynamics simulations.* Soft Matter, **9(29)**:6978–6985 (2013).

[45] W. Humphrey, A. Dalke and K. Schulten. *VMD: visual molecular dynamics.* J. Mol. Graph., **14(1)**:33–8, 27–8 (1996).

[46] P. Schaaf and J. Talbot. *Surface exclusion effects in adsorption processes.* J. Chem. Phys., **91(7)**:4401–4409 (1989).

[47] R. I. Masel. *Principles of adsorption and reaction on solid surfaces.* Wiley (1996).

[48] P. E. Scopelliti, A. Borgonovo, M. Indrieri et al. *The effect of surface nanometre-scale morphology on protein adsorption.* PLoS One, **5(7)**:1–9 (2010).

[49] T. C. Hales. *Historical Overview of the Kepler Conjecture.* Discrete Comput. Geom., **36(1)**:5–20 (2006).

[50] A. Rényi. *On a one-dimensional problem concerning random space-filling.* Publ. Math. Inst. Hung. Acad. Sci, **3**:109–127 (1958).

[51] H. Solomon and H. Weiner. *A Review of the Packing Problem.* Technical report, Stanford University (1986).

[52] Z. Adamczyk and P. Weronski. *Random sequential adsorption of spheroidal particles: Kinetics and jamming limit.* J. Chem. Phys., **105(13)**:5562–5573 (1996).

[53] H. Reiss and A. D. Hammerich. *Hard spheres: scaled particle theory and exact relations on the existence and structure of the fluid/solid phase transition.* J. Phys. Chem., **90(23)**:6252–6260 (1986).

[54] M. Deserno. *Fluid lipid membranes: From differential geometry to curvature stresses* (2014).

[55] M. Müller, K. Katsov and M. Schick. *Biological and synthetic membranes: What can be learned from a coarse-grained description?* Phys. Rep., **434(5-6)**:113–176 (2006).

[56] A. P. Lyubartsev and A. L. Rabinovich. *Recent development in computer simulations of lipid bilayers.* Soft Matter, **7(1)**:25 (2011).

[57] M. Venturoli, M. Maddalena Sperotto, M. Kranenburg et al. *Mesoscopic models of biological membranes* (2006).

[58] S. Pogodin and V. A. Baulin. *Coarse-grained models of phospholipid membranes within the single chain mean field theory.* Soft Matter, **6(10)**:2216 (2010).

[59] J. B. Freund. *Numerical Simulation of Flowing Blood Cells.* Annu. Rev. Fluid Mech, **46**:67–95 (2014).

[60] Y. Imai, T. Omori, Y. Shimogonya et al. *Numerical methods for simulating blood flow at macro, micro, and multi scales.* J. Biomech., **49**:2221–2228 (2016).

[61] J. Li, M. Dao, C. T. Lim et al. *Spectrin-level modeling of the cytoskeleton and optical tweezers stretching of the erythrocyte.* Biophys. J., **88(5)**:3707–3719 (2005).

[62] M. Dao, J. Li and S. Suresh. *Molecularly based analysis of deformation of spectrin network and human erythrocyte.* Mater. Sci. Eng. C, **26(8)**:1232–1244 (2006).

[63] W. G. Hoover. *Canonical dynamics: Equilibrium phase-space distributions.* Phys. Rev. A, **31(3)**:1695–1697 (1985).

[64] R. Kubo, M. Toda and N. Hashitsume. *Statistical Physics II*, volume 31 of *Springer Series in Solid-State Sciences.* Springer Berlin Heidelberg, Berlin, Heidelberg (1991).

[65] L. Verlet. *Computer "Experiments" on Classical Fluids. I. Thermodynamical Properties of Lennard-Jones Molecules.* Phys. Rev., **159(1)**:98–103 (1967).

[66] E. Vanden-Eijnden and G. Ciccotti. *Second-order integrators for Langevin equations with holonomic constraints.* Chem. Phys. Lett., **429(1-3)**:310–316 (2006).

[67] S. Plimpton. *Fast Parallel Algorithms for Short-Range Molecular Dynamics.* J. Comput. Phys., **117(1)**:1–19 (1995).

[68] E. Evans and Y. C. Fung. *Improved measurements of the erythrocyte geometry.* Microvasc. Res., **4(4)**:335–347 (1972).

[69] P.-O. Persson and G. Strang. *A Simple Mesh Generator in MATLAB.* SIAM Rev., **46(2)**:329–345 (2004).

[70] S. Suresh, J. Spatz, J. P. Mills et al. *Connections between single-cell biomechanics and human disease states: gastrointestinal cancer and malaria.* Acta Biomater., **1(1)**:15–30 (2005).

[71] M. P. Allen and D. J. Tildesley. *Computer simulation of liquids.* Clarendon Press (1989).

[72] P. C. Chou and N. J. Pagano. *Elasticity : tensor, dyadic, and engineering approaches.* Van Nostrand (1967).

[73] L. D. Landau, E. M. Lifshits, A. M. Kosevich et al. *Theory of elasticity.* Butterworth-Heinemann (1986).

[74] W. Helfrich. *Elastic Properties of Lipid Bilayers: Theory and Possible Experiments.* Zeitschrift für Naturforsch. C, **28(11-12)**:693–703 (1973).

[75] D. H. K. Nguyen, V. T. H. Pham, M. Al Kobaisi et al. *Adsorption of Human Plasma Albumin and Fibronectin onto Nanostructured Black Silicon Surfaces.* Langmuir, **32(41)**:10744–10751 (2016).

[76] N. L. Anderson and N. G. Anderson. *The human plasma proteome: history, character, and diagnostic prospects.* Mol. Cell. Proteomics, **1(11)**:845–67 (2002).

[77] I. Axelsson. *Characterization of proteins and other macromolecules by agarose gel chromatography.* J. Chromatogr. A, **152(1)**:21–32 (1978).

[78] A. Stukowski. *Visualization and analysis of atomistic simulation data with OVITO the Open Visualization Tool.* Model. Simul. Mater. Sci. Eng., **18(1)**:015012 (2010).

[79] C. Runge. *Ueber die numerische Auflsung von Differentialgleichungen.* Math. Ann., **46(2)**:167–178 (1895).

[80] Kutta. *Beitrag zur näherungweisen Integration totaler Differentialgleichungen.* Ph.D. thesis, Munich (1901).

[81] B. M. Rothen-Rutishauser, S. Schürch, B. Haenni et al. *Interaction of fine particles and nanoparticles with red blood cells visualized with advanced microscopic techniques.* Environ. Sci. Technol., **40(14)**:4353–9 (2006).

UNIVERSITAT
ROVIRA i VIRGILI

SEVENTH FRAMEWORK
PROGRAMME

MARIE CURIE ACTIONS